# DISCLAIMER

This report was prepared as an account of work sponsored by an agency of the United States Government. Neither the United States Government nor any agency thereof, nor any of their employees, makes any warranty, express or implied, or assumes any legal liability or responsibility for the accuracy, completeness, or usefulness of any information, apparatus, product, or process disclosed, or represents that its use would not infringe privately owned rights. Reference herein to any specific commercial product, process, or service by trade name, trademark, manufacturer, or otherwise does not necessarily constitute or imply its endorsement, recommendation, or favoring by the United States Government or any agency thereof. The views and opinions of authors expressed herein do not necessarily state or reflect those of the United States Government or any agency thereof. Reference herein to any social initiative (including but not limited to Diversity, Equity, and Inclusion (DEI); Community Benefits Plans (CBP); Justice 40; etc.) is made by the Author independent of any current requirement by the United States Government and does not constitute or imply endorsement, recommendation, or support by the United States Government or any agency thereof.

ANL-AMMT-024

# The effect of heat treatment on the defect evolution in LPBF 316H stainless steel

---

Nuclear Science and Engineering Division

**About Argonne National Laboratory**
Argonne is a U.S. Department of Energy laboratory managed by UChicago Argonne, LLC under contract DE-AC02-06CH11357. The Laboratory's main facility is outside Chicago, at 9700 South Cass Avenue, Argonne, Illinois 60439. For information about Argonne and its pioneering science and technology programs, see www.anl.gov.

**DOCUMENT AVAILABILITY**

**Online Access:** U.S. Department of Energy (DOE) reports produced after 1991 and a growing number of pre-1991 documents are available free at OSTI.GOV (http://www.osti.gov/), a service of the US Dept. of Energy's Office of Scientific and Technical Information.

**Reports not in digital format may be purchased by the public from the National Technical Information Service (NTIS):**
U.S. Department of Commerce
National Technical Information Service 5301
Shawnee Rd
Alexandria, VA 22312
**www.ntis.gov**
Phone: (800) 553-NTIS (6847) or (703) 605-6000
Fax: (703) 605-6900
Email: **orders@ntis.gov**

**Reports not in digital format are available to DOE and DOE contractors from the Office of Scientific and Technical Information (OSTI):**
U.S. Department of Energy
Office of Scientific and Technical Information
P.O. Box 62
Oak Ridge, TN 37831-0062
**www.osti.gov**
Phone: (865) 576-8401
Fax: (865) 576-5728
Email: **reports@osti.gov**

**Disclaimer**
This report was prepared as an account of work sponsored by an agency of the United States Government. Neither the United States Government nor any agency thereof, nor UChicago Argonne, LLC, nor any of their employees or officers, makes any warranty, express or implied, or assumes any legal liability or responsibility for the accuracy, completeness, or usefulness of any information, apparatus, product, or process disclosed, or represents that its use would not infringe privately owned rights. Reference herein to any specific commercial product, process, or service by trade name, trademark, manufacturer, or otherwise, does not necessarily constitute or imply its endorsement, recommendation, or favoring by the United States Government or any agency thereof. The views and opinions of document authors expressed herein do not necessarily state or reflect those of the United States Government or any agency thereof, Argonne National Laboratory, or UChicago Argonne, LLC.

**ANL-AMMT-024**

# The effect of heat treatment on the defect evolution in LPBF 316H stainless steel

---

**Wei-Ying Chen, Yiren Chen, Peter Baldo, Jiaxuan Li**
Nuclear Science and Engineering Division
Argonne National Laboratory

**Dzmitry Harbaruk**
Experimental Operations and Facilities Division
Argonne National Laboratory

**Gyuchul Park**
Chemical and Fuel Cycle Technology Division
Argonne National Laboratory

**Stephen Taller**
Fusion and Fission Energy Sciences Directorate
Oak Ridge National Laboratory,

September-30-2025

# ABSTRACT

This work investigates the effect of processing and heat treatment condition on defect evolution and irradiation response of laser powder bed fusion (LPBF) 316H stainless steel, with comparisons to LPBF 316L and wrought 316L/316H. Using *in-situ* and *ex-situ* ion irradiations across a wide parameter space, we correlated void swelling, dislocation loop evolution, and segregation behavior with pre-irradiation microstructures. Our results show that swelling is strongly influenced by prior-irradiation dislocation density: an intermediate dislocation density maximizes swelling in LPBF materials, while both low and high dislocation densities reduce it to the level comparable to those of wrought alloys. Low dose rates and helium both promote cavity nucleation and therefore shorten the incubation period, with helium suppressing the role of dislocation density and driving swelling behavior toward a response similar to that of wrought materials. Dislocation loop evolution in solution annealed LPBF 316H resembles that of wrought 316H but shows localized denuded zones near low-angle grain boundaries. STEM-EDS mapping further revealed Ni segregation at voids and sparse Al-rich oxides, without evidence of Ni–Si precipitates. Collectively, these findings identify dislocation density, helium content, and dose rate as the factors governing swelling in LPBF 316H and provide datasets for mechanistic model validation, supporting Licensing Approach with Ions and Neutrons (LAIN) and the qualification of additive manufactured (AM) austenitic steels for nuclear service.

# TABLE OF CONTENTS

# LIST OF FIGURES

# LIST OF TABLES

# 1 Introduction

The emergence of metal additive manufacturing (AM) has opened new pathways for advancing material technologies. AM enables rapid and cost-effective productions of components with complex geometries, leading to innovations across the field of materials science and manufacturing technologies. As a result, AM materials have received significant attention as a means of producing high-quality components with enhanced design flexibility and customization. While the chemical compositions of AM materials are often similar to their traditionally manufactured counterparts, they possess distinct microstructures. Microstructural features introduced during the printing process, such as porosity, anisotropic grain structures, inclusions, dislocation cells, and chemical inhomogeneities—are commonly observed in AM materials. These microstructures, along with their behavior under service conditions, must be thoroughly evaluated before AM materials can be widely adopted.

To accelerate the development of advanced materials and manufacturing technologies, the Advanced Materials and Manufacturing Technologies (AMMT) program within the Department of Energy's Office of Nuclear Energy (DOE NE) is focusing on evaluating the performance of AM materials in nuclear applications. Understanding how these materials respond to irradiation in reactor environments is essential for ensuring the reliability and safety of nuclear components. As with any new reactor material, AM materials require careful assessment of their irradiation response. Certain microstructural features unique to AM materials, such as compositional inhomogeneity and dislocation cells, are of particular interest because they may impact the materials' irradiation performance.

Ion irradiation is a valuable method for studying the irradiation response of AM materials. Compared to neutron irradiation, ion irradiation is readily accessible, produces little to no radioactivity in samples, and allows for precise controls over irradiation condition and environment. Additionally, ion irradiation can induce displacement damage quickly, reducing time required to achieve high damage levels. This enables rapid screening and exploration of various AM printing and post-processing conditions with respect to irradiation damage. However, the lower damage rates and helium transmutation in reactor irradiation can lead to microstructural evolution that differs from those caused by ion irradiation. Therefore, modeling and simulation play a critical role in bridging these differences, helping transform ion irradiation results to meaningful predictions of material performance under neutron irradiation in reactors. It is essential to understand the phenomena that are accelerated, altered, or absent under ion irradiation in order to effectively use these results for forecasting the service behavior of materials in nuclear environments.

During the previous fiscal year (FY) [1], we investigated the irradiation performance of LPBF 316L (0.006 wt% C) and LPBF 316H (0.04 wt% C) stainless steels (SS), and their wrought counterparts. The research involved fabricating, preparing, irradiating, and characterizing six materials: two variants of LPBF 316L, two variants of LPBF 316H, and wrought 316L and 316H SS. LPBF materials were subjected to various heat treatments, including solution annealing and stress relief, and were irradiated using *in-situ* and *ex-situ* ion techniques at temperatures of 300°C and 600°C, with doses ranging from 0.2 dpa to 25 dpa. The characterization of irradiated materials focused on the as-built condition, with an emphasis on the effects of carbon and pre-existing dislocation cell structure.

This FY, we shifted our focus to the effect of processing conditions — as-built (AB), solution annealing (SA), stress relief (SR), cold working (CW) and wrought — on the defect evolution of LPBF 316H (0.08 wt%) SS. The objective was twofold: (1) to rapidly assess the irradiation responses of various processing conditions and identify the key factors influencing their performance under irradiation, and (2) to generate high-fidelity data to support the development of irradiation damage models for AM materials to correlate ion and neutron irradiation outcomes [2, 3]. The ultimate goal of this effort is to support the AMMT's goal of using combined neutron and ion irradiation data to accelerate the qualification of AM materials for nuclear applications — Licensing Approach with Ions and Neutrons (LAIN) [4].

# 2 Experimental

The experimental methods and procedures are discussed in this section. Section 2.1 describes the materials and their pre-irradiation heat treatments. Section 2.2 discusses the *in-situ* ion irradiation experiments. Section 2.3 discusses the *ex-situ* ion irradiation experiments. Section 2.4 discusses the procedure of post-irradiation sample preparation and microstructural characterization of *ex-situ* irradiated samples.

## 2.1 Materials and pre-irradiation specimen preparations

Five materials have been investigated in this work package since FY23 designated as LPBF316L-1, LPBF316H-1, LPBF316H-2, wrought 316L and wrought 316H. The measured compositions of the AM materials and the ASTM composition of the wrought materials are given in Table 1. These AM prints were produced with LPBF at two laboratories. The LPBF316L-1 and LPBF316H-2 were printed at Oak Ridge National Laboratory (ORNL) using a Concept Laser M2 system by GE [5, 6]. The LPBF316H-1 were printed at ANL using a Renishaw AM400 system [7]. Some ion irradiation results for LPBF316L-1 and LPBF316H-1 have been reported previously [1, 8]. The LPBF316L-1 was neutron-irradiated in High Flux Isotope Reactor (HFIR) by Transformational Challenge Reactor program [9]. The neutron irradiation for LPBF316H-2 is ongoing under AMMT program in HFIR and Advanced Test Reactor (ATR) [10, 11]. The compositions of LPBF316L-1and LPBF316H-2 shown in Table 1 are the nominal composition of the powder provided by vendors. The post-printing composition of LPBF316H-1 was measured by cutting a small piece from the build and analyzing with combustion infrared detection for carbon, inert gas fusion for hydrogen, oxygen and nitrogen, and direct current plasma emission spectroscopy for other elements.

Table 2 shows the heat treatment conditions investigated for each material. The as-built (AB) condition was investigated for LPBF 316L-1, LPBF316H-1 and LPBF 316H-2. For LPBF 316L-1 and LPBF316H-1, SA was performed by ANL with disk samples wrapped in Ta foil and then vacuum encapsulated inside a quartz tube. The tube was heated in a furnace at 1100°C for 1 hour followed by air cooling. For LPBF316H-2, SA at 1200°C for 2 hours and SR at 650°C for 24 hours were performed at ORNL in air furnace, followed by water quenching and air cooling, respectively. A small block of AB LPBF 316H-2 was cold-worked (CW) to 20% at University of Illinois, Urbana-Champaign.

The printed materials were machined into 3-mm-diameter rods using an electrical discharge machine (EDM) along build direction. Then, the rods were cut into 0.5 mm-thick disks with EDM or 0.6-1 mm-thick disks with slow speed saw. For SA and SR LPBF316H-2 specimens, disks were extracted from different height from the bottom of the print. For *in-situ* ion irradiations, the disks were mechanically polished on both sides with sandpapers to a thickness around 100 μm, and then electropolished between -30ºC and -40ºC with a voltage of 28V until perforation using a Struers Tenupol-5 polisher. The electrolyte used was a 5% perchloric acid solution in methanol. For *ex-situ* ion irradiations, only one side of the disks was polished. The polishing was performed with sandpapers down to P4000 grit, polycrystalline diamond suspension down to 1 μm, vibratory polishing using 50 nm colloidal silica polishing suspension, and finally electropolishing at -30ºC to -40ºC using the same electrolyte for 20-30 seconds. After electropolishing, samples were rinsed through 3 batches of methanol at room temperature. Following the last rinse, each disk was placed on filter paper to quickly drain residual methanol and minimize potential contamination that could remain upon evaporation. Samples were stored in a desiccator prior to irradiation.

Table 1. Compositions of the LPBF316L and LPBF316H stainless steels in this study

| Materials | LPBF 316L-1 (Powder) | | 316L (Wrought) | | 316H (Wrought) | | LPBF 316H-1 (Print) | | LPBF 316H-2 (Powder) | |
|---|---|---|---|---|---|---|---|---|---|---|
| Build ID | 20190308 | | ASTM A240 | | ASTM A240 | | 20220217M | | B1P6 | |
| | wt% | at% | wt% | at%* | wt% | at%* | wt% | at% | wt% | at% |
| Oxygen | 0.05 | 0.174 | - | - | - | - | 0.046 | 0.16 | 0.03 | 0.105 |
| Nitrogen | 0.01 | 0.04 | - | - | - | - | 0.015 | 0.06 | 0.01 | 0.04 |
| Carbon | 0.006 | 0.028 | < 0.03 | < 0.139 | 0.04 - 0.1 | 0.185 - 0.461 | 0.04 | 0.185 | 0.08 | 0.371 |
| Sulfur | - | - | 0.03 | 0.052 | 0.03 | 0.052 | 0.005 | 0.009 | 0.0 | 0.0 |
| Iron | Bal. | Bal. | Bal. | Bal. | Bal. | Bal. | Bal. | Bal. | Bal. | Bal. |
| Chromium | 17.1 | 18.3 | 16 - 18 | 18.2 | 16 - 18 | 18.2 | 17.04 | 18.23 | 17.0 | 18.224 |
| Manganese | 1.19 | 1.21 | 2 | 2.02 | 2 | 2.02 | 1.09 | 1.10 | 1.05 | 1.065 |
| Silicon | 0.46 | 0.912 | 0.75 | 1.48 | 0.75 | 0.148 | 0.45 | 0.891 | 0.07 | 0.139 |
| Nickel | 12.1 | 11.5 | 10 - 14 | 11.35 | 10 - 14 | 11.35 | 12.22 | 11.58 | 12.3 | 11.68 |
| Copper | 0.01 | 0.009 | - | - | - | - | 0.007 | 0.006 | - | - |
| Molybdenum | 2.41 | 1.40 | 2 - 3 | 1.45 | 2 - 3 | 1.45 | 2.57 | 1.49 | 2.3 | 1.34 |
| Vanadium | - | - | - | - | - | - | 0.01 | 0.011 | - | - |
| Phosphorus | <0.005 | <0.009 | 0.045 | 0.08 | 0.045 | 0.08 | 0.018 | 0.032 | < 0.005 | < 0.009 |
| Cobalt | 0.1 | 0.094 | - | - | - | - | 0.028 | 0.026 | - | - |
| Tungsten | - | - | - | - | - | - | < 0.002 | < 0.001 | - | - |

* Use Cr = 17wt%, Ni = 12 wt%, and Mo = 2.5 wt% for calculation

Table 2. Materials of Examination

| Label | Lab printed - Build number | Processing Condition |
|---|---|---|
| LPBF316L-1 | ORNL [6]<br>- 20190308 | • As-built<br>• Solution annealed (1100ºC, 1 hr) |
| LPBF316H-1 | ANL [12]<br>- 20220217M | • As-built<br>• Solution annealed (1100ºC, 1 hr) |
| LPBF316H-2 | ORNL [5]<br>- B1P7-R (AB)<br>- P6b (SA)<br>- P6a (SR) | • As-built<br>• As-built + 20% cold working<br>• Stress relieved (650 °C, 24 hr)<br>• Solution annealed (1200°C, 2 hr) |
| W316L | ORNL<br>-HT-SC48038/PL-52539 | • Annealed wrought material. |
| W316H | ORNL<br>- 8092297 | • Annealed wrought material. |

## 2.2 *In-situ* ion irradiations

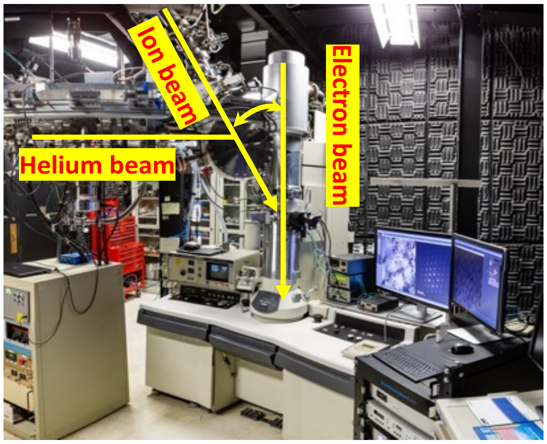

Figure 1. The IVEM-Tandem Facility in Argonne National Laboratory

*In-situ* ion irradiations were performed at the Intermediate-Voltage Electron Microscope (IVEM) Facility at ANL using a NEC implanter and a Hitachi-9000 TEM (Figure 1) [13]. The ion beam was bent through a magnet and a deflector before entering the microscope with an angle of 30° with respect to the electron optical axis. The microscope was operated at 300 kV to allow electron transparency for the thicker region of the specimen foil. The vacuum was measured with a cold-cathode gauge positioned near the specimen holder and was maintained between $5\times10^{-8}$ to $3\times10^{-7}$ torr throughout the experiments. A Gatan double-tilt heating holder (model 652) was used to control the specimen temperature and to tilt the specimen to the desired crystalline orientation. During irradiation, the specimen holder was tilted about 15° toward the ion beam. Before irradiation, the current was measured using a Faraday catch cup located about 5 cm above the sample. The ion flux was calculated by dividing this current by the size of the limiting aperture positioned upstream. During irradiation, the catch cup was removed, and the current was monitored using a skim cup placed between the sample and the limiting aperture. The ion beam was slightly rastered to achieve a uniform intensity across the irradiation area.

The irradiation parameters for the *in-situ* experiments since FY23 are given in Table 3. $Kr^{2+}$ ions with an energy of 1 MeV and $6.3\times10^{11}$ ions/cm$^2$ flux were used for all experiments. This flux corresponds to a dose rate of $10^{-3}$ dpa/s, as calculated by SRIM [14] at a depth of 100 nm in quick calculation mode ([15]). For all samples, the irradiation was paused for taking images and diffraction patterns at designated dose steps. Bright-field (BF) and dark-field (DF) images were taken in two-beam conditions with g = 200 near (011) or (001) zone axes. Cavities and precipitates were imaged in BF with defocused conditions. For experiments with irradiation temperatures above 500°C, the temperatures were reduced to 250-350°C during image acquisition. Lowering temperature reduced the thermal annealing effect on the irradiation-induced defects and minimize the oxidation potential of foil surface. It also enhanced the image quality. The final fluence for an irradiated sample was either $3.1\times10^{15}$ ions/cm$^2$ (5 dpa) or $6.3\times10^{14}$ ions/cm$^2$ (1 dpa). Sample's microstructural data at the final fluence was taken at room temperature.

Table 3 lists all in-situ ion irradiation experiments since FY23. In FY25, an experiment on wrought 316L was performed at a higher temperature of 650°C to extend the dataset to higher temperatures. In addition, an experiment on SA LPBF316H-2 (0.08 wt%) was performed at 600°C to 1 dpa to investigate the carbon effect by comparing with SA LPBF316H-1 (0.04 wt.%).

**Table 3**. Irradiation matrix of *in-situ* ion irradiation

| Materials | Heat Treatment | Temp (°C) | Flux/ Fluence |
|---|---|---|---|
| LPBF316L-1 | AB | 300<br>600 | $6.25\times10^{11}$ ions/cm$^2$/s ($10^{-3}$ dpa/s)<br>$3.1\times10^{15}$ ions/cm$^2$ (5 dpa) |
| LPBF316H-1 | AB | | |
| | SA | 600 | $6.25\times10^{11}$ ions/cm$^2$/s ($10^{-3}$ dpa/s)<br>$6.3\times10^{14}$ ions/cm$^2$ (1dpa) |
| Wrought 316L | W | 500, 600, 625, 650* | |
| LPBF316H-2* | SA | 600 | $6.25\times10^{11}$ ions/cm$^2$/s ($10^{-3}$ dpa/s)<br>$6.3\times10^{14}$ ions/cm$^2$ (1dpa) |

* FY25 work package

## 2.3 *Ex-situ ion* irradiations

*Ex-situ* ion irradiations were performed using the Tandem accelerator at the *ex-situ* beam lines of IVEM facility. The ion beam was bent through a magnet before entering the specimen chamber. The dosimetry was conducted with a (rear) Faraday cup behind the specimen and an annular Faraday cup in front of the specimen. The beam current through a 3-mm diameter aperture was measured by the rear Faraday cup before, after, and if necessary, during the irradiation if beam conditions changed. When the ion beam was on target, current was monitored and integrated with an annular Faraday cup in the front of the chamber. Right before an irradiation experiment, the specimen and the holder were cleaned using a Fischione nanoClean plasma cleaner model 1070 for 5 minutes at the Center for Nanoscale Materials (CNM) of ANL.

The size of the rear aperture of the annular Faraday cup is 3 mm in diameter. The fluxes for 4 MeV $Ni^{2+}$ and 5 MeV $Ni^{2+}$ ions were $1.72\times10^{12}$ ions/cm$^2$/s and $2.15\times10^{12}$ ions/cm$^2$/s, respectively, which corresponds to current readouts of 39 nA and 46 nA, respectively, on the rear Faraday cup. Based on the SRIM calculation, as shown in Figure 2(a), which was calculated based on $^{58}$Co instead of $^{58}$Ni due to an error in the SRIM database of this specific isotope, these fluxes give a dose rate of $10^{-3}$ dpa/s at a depth of 600 nm 5 MeV $Ni^{2+}$ ion irradiations. During irradiation, beam stability was monitored by the current readout on the annular Faraday cup.

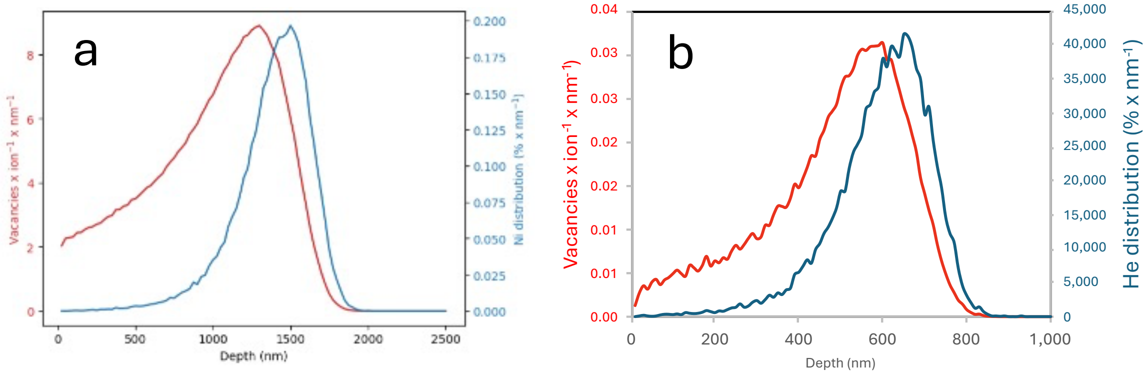

Figure 2. SRIM calculation of (a) 5 MeV Co (simulating 5 MeV $Ni^{2+}$) with normal angle and (b) 325 keV He ions into Type 316 stainless steels with 31° incident angle.

The 3-mm specimen was clamped in a stainless-steel holder. The sample was held in place by a Ta disk backed by a set screw. The sample holder was attached to a heating block containing a 400-Watt quartz halogen lamp. A type K thermocouple was attached to the surface of the sample holder. The irradiation chamber was pumped by an ion pump as well as by a maglev turbo pump backed by a scroll pump. Vacuum, measured with an ion gauge, varied between the mid $10^{-8}$ Torr range for 300°C irradiations and the low $10^{-7}$ Torr range for 600°C irradiations. Table 4 shows all single-beam irradiations performed since FY23 using 4 MeV $Ni^{2+}$ and 5 MeV $Ni^{2+}$ ions. Irradiations in FY25 focused on LPBF316H-2 with various processing conditions. The irradiation matrix was designed to reveal the dependence on dose and temperature, and the differences between those processing conditions.

In addition to single-beam irradiation, dual-beam irradiations were performed with concurrent 5 MeV $Ni^{2+}$ and 325 keV $He^{+}$ ions at 600°C. Figure 3 shows the top view of the ex-situ irradiation chamber for dual-beam irradiation. Table 5 listed the conditions of dual-beam irradiations on SA and SR LPBF316H-2. The 5 MeV $Ni^{2+}$ ions were produced from Tandem accelerator using the same setup as in the single-beam irradiation. The 325 keV $He^{+}$ ions were produced from the 500 kV implanter. The dosimetry for the 325 keV $He^{+}$ beam is composed of a (rear) Faraday cup behind the specimen and an annular Faraday cup in front of the specimen. The beam current through the 5 mm diameter aperture was measured by the rear Faraday cup before, after, and if necessary, during the irradiation if beam conditions changed. When beam was on target, current was monitored and integrated with an annular Faraday cup in the front of the chamber. Two fluxes for 325 keV $He^{+}$

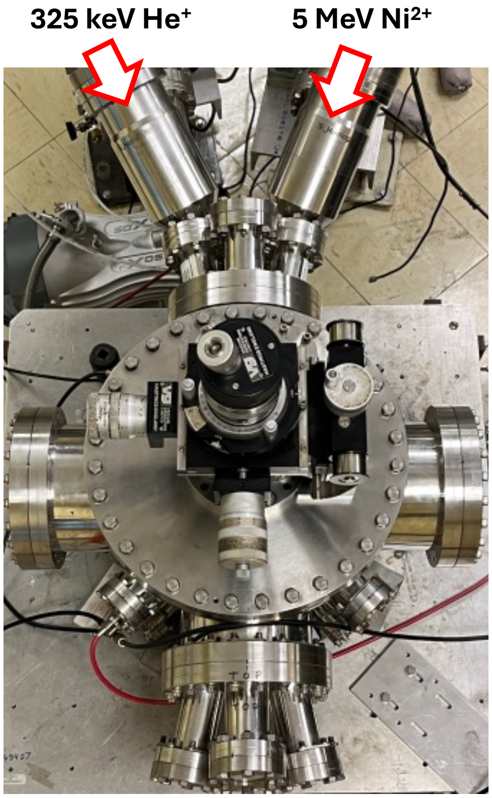

Figure 3. Irradiation station of *ex-situ* dual-beam ion irradiation.

ions were performed, resulting in He/dpa ratios of 250 appm He/dpa (250 appm He/dpa) and 25 appm He/dpa (0.0025% He/dpa) where the corresponding currents were 15 nA and 1.5 nA, respectively.

The incident angles between the $Ni^{2+}$ ions and $He^{+}$ ions with the sample normal were 10° and 31°, respectively. Figure 2(b) shows the SRIM calculation 325 keV He ion irradiation into 316 SS with an incident angle of 31°. A flux of $2.15\times10^{12}$ ions/cm$^2$/s for 5 MeV $Ni^{2+}$ ions leads to a dose rate of $10^{-3}$ dpa/s at a depth of 600 nm in 316 stainless steel, which is also the peak implantation depth for 325 keV $He^{+}$ ions with an incident angle of 31°. SA and SR LPBF 316H-2 were also dual-beam irradiated in Michigan ion beam laboratory (MIBL) in University of Michigan with 9 MeV $Fe^{3+}$ and 3.42 MeV $He^{2+}$ ions. A nominally 6 µm Al foil was used as an energy degrader was used for $He^{2+}$ ions to have a consistent He concentration from 600 nm to 1500 nm. The flux and fluence (Table 5) were designed to achieve 10 dpa and 20 appm He with a dose rate of $10^{-3}$ dpa/s at a depth of 1 µm. Figure 4 shows the corresponding SRIM calculation of 316 stainless steel irradiated under the same He/dpa ratio.

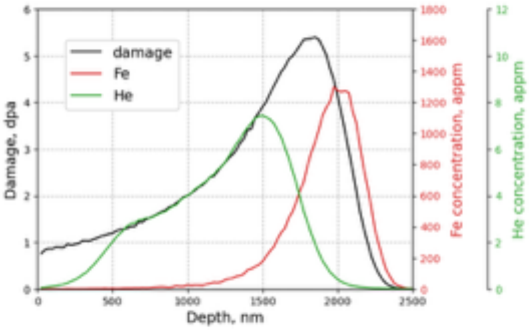

Figure 4. SRIM calculation of (a) 9 MeV $Fe^{3+}$ and 3.42 MeV keV $He^{2+}$ ions into Type 316 stainless steels with energy degrader for $H^{2+}$ ions.

Additionally, lower dose rate ($10^{-5}$ dpa/s) irradiations were performed in MIBL on SA and SR LPBF 316H-2 and W316H at 600°C to 2 dpa with 9 MeV $Fe^{3+}$ ions as shown in Table 6. The low dose-rate ($10^{-5}$ dpa/s) data is compared with high dose-rate ($10^{-3}$ dpa/s) data for studying the dose rate effect and providing data to develop models to bridge the gap between ion and neutron irradiations. The MIBL beamline setup can be found in Ref. [16, 17].

## 2.4 Post-irradiation microstructure characterization

Two methods were used to prepare the TEM specimens of ex-situ irradiated samples: electropolishing and focused ion beam (FIB). The electropolishing procedure has been described in detail in FY24 report [1]. The FIB lift-out was carried out using a Thermal Fisher Scientific Helios 5 CX Ga-FIB at CNM. Cross-sectional specimens prepared by FIB lift-out were used for void-swelling studies on samples irradiated to 5 dpa and 10 dpa. For imaging, the specimens were first tilted to orientations that minimized overall contrast from the dislocation structures. Voids were then imaged in bright field (BF) with under-focused and over-focused conditions at magnifications of 30kx with 1 µm and 5 µm defocus for observing the void distribution across the entire irradiation range and 100kx with 650 nm defocus to examine greater detail at a depth of 600 nm from the surface. The diameter of the voids is reported as the size.

Table 4. Single Ion Beam *ex-situ* Irradiation Condition

| Materials | Ion | Temp (°C) | Dose rate (dpa/s) | Dose (dpa) |
|---|---|---|---|---|
| LPBF316L-1 AB | 4 MeV $Ni^{2+}$ | 600 | $10^{-3}$ | 0.2, 2, 5, 10, 25 |
| | | | $10^{-4}$ | 0.2, 2 |
| | | | $10^{-5}$ | 0.2 |
| | | 300 | $10^{-3}$ | 0.2, 2, 5, 10, 25 |
| | | | $10^{-4}$ | 0.2, 2 |
| | | | $10^{-5}$ | 0.2 |
| LPBF316L-1 SA | | 300, 600 | $10^{-3}$ | 0.2, 2, 5, 10 |
| Wrought 316L | 5 MeV $Ni^{2+}$ | 300, 400, 500, 600 | | 10 |
| | | 300, 600 | | 2 |
| Wrought 316H | | 300, 400, 500, 600 | | 10 |
| | | 400, 600 | | 0.5, 2 |
| LPBF316H-1 AB | 4 MeV $Ni^{2+}$ | 300, 600 | | 0.2, 2, 5, 10 |
| LPBF316H-2 AB* | 5 MeV $Ni^{2+}$ | 550, 575, 600, 625, 650, 675 | | 10 |
| | | 600 | | 0.5, 5, 10, 15 |
| LPBF316H-2 AB+CW* | | 600 | | 10 |
| LPBF316H-2* SR | | 400 | | 0.2, 2, 5, 10 |
| | | 600 | | 0.2, 0.5, 2, 5, 10, 15 |
| | | 400, 500, 600, 650 | | 10 |
| LPBF316H-2* SA | | 300, 400, 500, 600, 650 | | 10 |
| | | 300, 400, 500 | | 0.5, 2, 10 |
| | | 600 | | 0.5, 2, 5, 7.5, 10, 15 |

[*] FY25 work package

Table 5. Dual Ion Beam ex-situ Irradiation Condition

| **Materials** | **Ion** | **Temp (°C)** | **Dose rate (dpa/s) (% He/dpa)** | **Dose (dpa)** |
|---|---|---|---|---|
| LPBF316H-2 SR | 5 MeV $Ni^{2+}$ + 325 keV $He^{+}$ | 600 | $10^{-3}$ (from Ni ions) 250 appm-0.0025% He/dpa | • 10 dpa + 250 appm He<br>• 10 dpa + 2500 appm He |
| LPBF316H-2 SA | | | | • 10 dpa + 250 appm He<br>• 10 dpa + 2500 appm He<br>• 2500 appm He only |
| LPBF316H-2 SA and SR | 9 MeV $Fe3^{+}$ + 3.42 MeV $He^{2+}$ (with degrader) | | $10^{-3}$ (from Fe ions) 0.0002% He/dpa | • 10 dpa + 20 appm He |

Table 6. Low Dose-Rate Irradiations

| **Materials** | **Ion** | **Temp (°C)** | **Dose rate (dpa/s)** | **Dose (dpa)** |
|---|---|---|---|---|
| W316H | 9 MeV $Fe^{3+}$ | 600 | $10^{-5}$ | 2 dpa |
| LPBF316H-2 SR | | | | |
| LPBF316H-2 SA | | | | |

# 3 Results and Discussion

## 3.1 TEM examinations of materials before irradiation

This section presents the TEM characterization of the microstructures corresponding to the four processing conditions of LPBF 316H-2.Figure 5 displays the BF TEM image of AB LPBF 316H-2. A typical dislocation cell structure, consistent with other as-built LPBF 316 stainless steels [18], is observed. No $M_{23}C_6$ precipitates were detected by electron diffractions. Figure 6 shows BF TEM images and the associated diffraction pattern of SR LPBF 316H-2. While the dislocation cell structure is retained, its density is reduced compared to the as-built condition. $M_{23}C_6$ precipitates are observed decorating the dislocation cell walls, as confirmed by diffraction spots in Figure 6 (d). Stacking fault tetrahedra (SFTs) are visible in Figure 6(c), with yellow arrow A indicating dissociated dislocations in Figure 6(b).

Figure 7 and Figure 8 illustrate low- and high-magnification TEM images, respectively, of SA LPBF 316H-2. The low-magnification images in Figure 7 reveal that the original dislocation cell structure has been replaced by small grains. In Figure 7(a), the small grains on the right side are comparable in size to typical dislocation cells in LPBF 316 SS, suggesting a correlation between dislocation cells and new grains. Figure 7(b) and Figure 7(c) show a slight increase in grain size, indicating possible grain growth. Figure 7(d) reveals a region of high dislocation density, suggesting that the solution annealing process did not fully eliminate dislocations, although they no longer form well-defined cell structures.

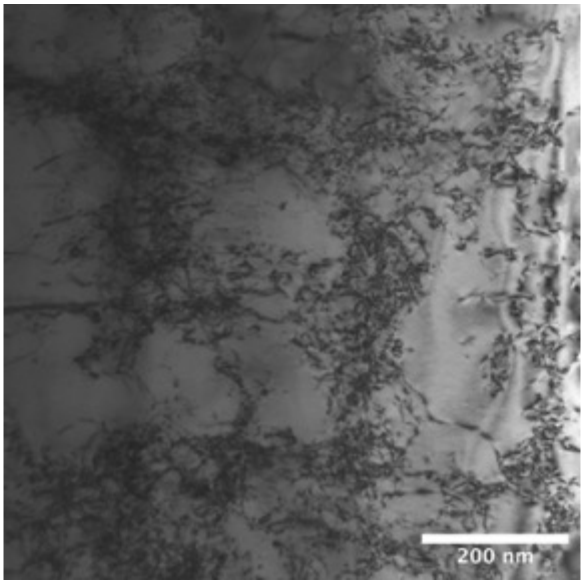

Figure 5. BF TEM image of as-received AB LPBF 316H-2. The image was taken near [011] with g = 002.

High-magnification DF TEM images in Figure 8 offer further insight into dislocation configurations. In Figure 8(a), yellow arrows A mark dissociated dislocations, while arrows B highlight aligned dislocations, indicating the beginning of low-angle grain boundary formation. This alignment suggests that during high-temperature solution annealing, dislocations within the original cell walls reorganized into lower-energy configurations. This process likely led to the formation of low-angle grain boundaries, as indicated by yellow arrow C in Figure 8(b) and Figure 8(c). The misorientation across the boundary appears more pronounced in Figure 8(c) than in Figure 8(b). No carbides were observed at the grain boundaries, nor were they detected in the diffraction patterns.

Figure 9(a)–Figure 9(c) show BF TEM images of 20% CW LPBF 316H-2 at increasing magnifications. Cold working introduced deformation features such as slip bands and a noticeable increase in dislocation density. The corresponding diffraction pattern in Figure 9(d) indicates retention of the austenitic phase, with no evidence of $M_{23}C_6$ precipitation or deformation-induced martensite.

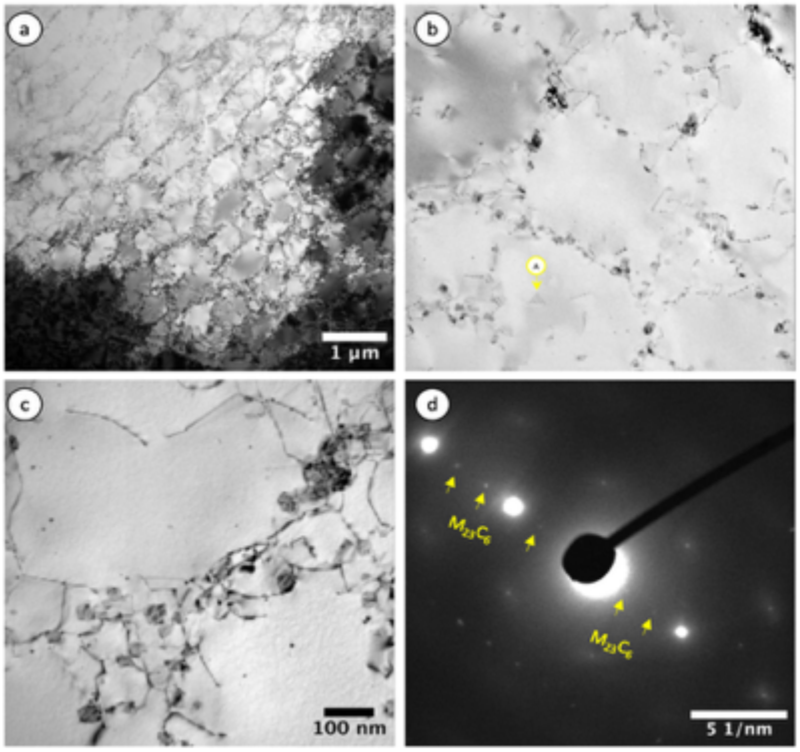

Figure 6. (a-c) TEM images of as-received SR LPBF316H-2 with magnification increasing from. (d) diffraction pattern taken near [110] with g = 200.

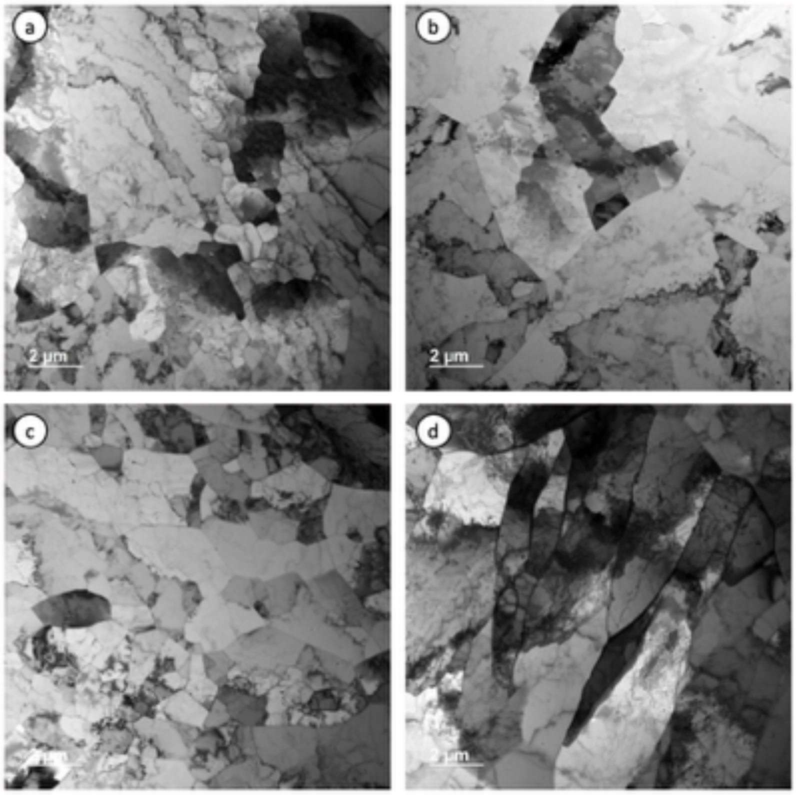

Figure 7. Low magnification BF TEM images of SA LPBF 316H-2

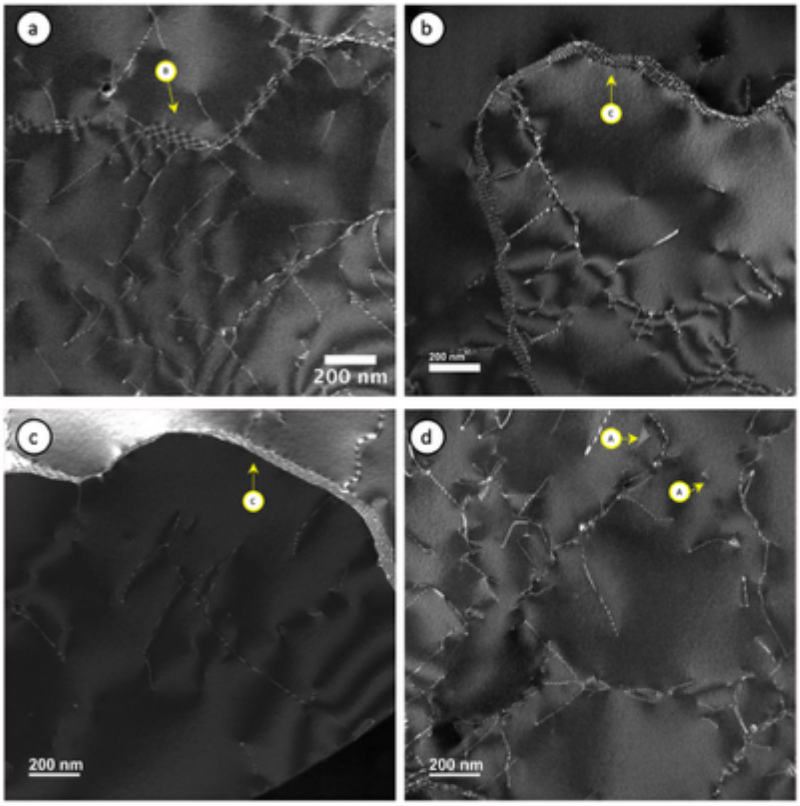

Figure 8. Higher magnification DF images of as-received SA LPBF 316H-2

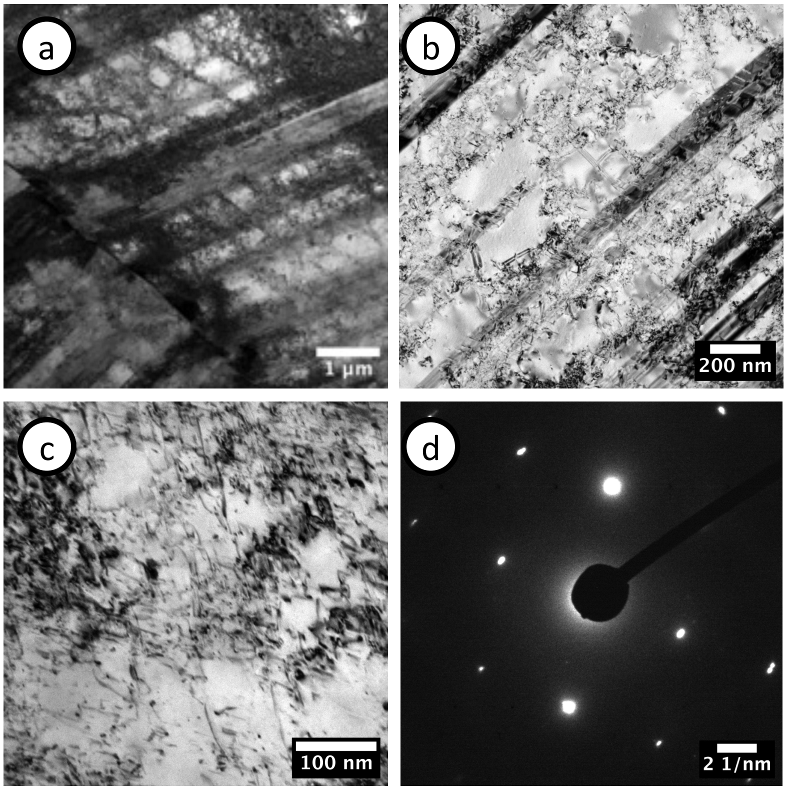

Figure 9. BF (a-c) TEM images of as-received 20% cold-worked SA LPBF 316H-2 with increasing magnification. (d) Diffraction pattern.

In summary, the microstructures of LPBF 316H-2 under four post printing treatment conditions were characterized using TEM. The relative dislocation density follows the order: 20% CW > AB > SR > SA. Dislocation cell structures are clearly evident in both AB and SR materials. In the 20% CW condition, the cell structure persists but is partially obscured by deformation-induced slip bands. In the SA condition, the original dislocation cell structure is eliminated—either through dislocation annihilation, reorganization into lower-energy configurations, or replacement by recrystallized grains. $M_{23}C_6$ carbides were observed only in the SR condition and were absent in all others.

The TEM images of AB LPBF 316H-1 and SA LPBF 316H-1 are shown in Figure 10 and Figure 11, respectively. Similar to the transition of LPBF 316H-2 from AB to SA, the microstructure was transformed from dislocation cell structure to a mixture of recrystallized small grains and larger grains with higher dislocation density. The remaining dislocation density in SA LPBF 316H-1 remained considerable, as evidenced in Figure 11(c), and appeared to be higher than that in SA LPBF 316H-2, likely due to the lower annealing temperature (1100 °C vs. 1200 °C) and lower annealing time (1 hour vs 2 hour).

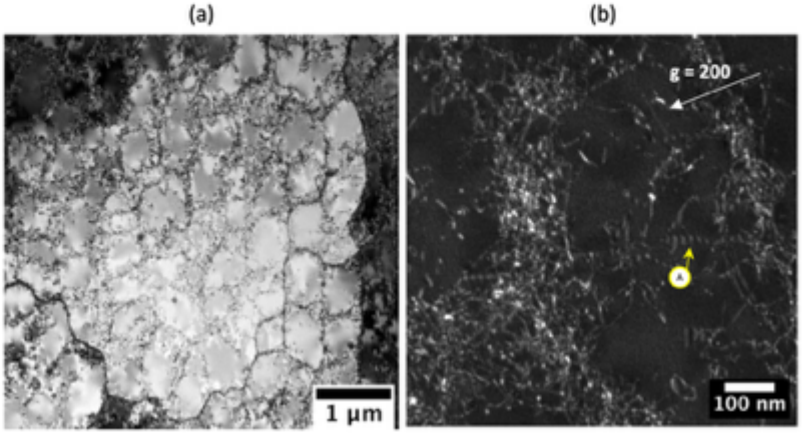

**Figure 10**. TEM images of as-built LPBF 316H-1: (a) low-magnification BF TEM image. (b) high-magnification DF TEM image in two-beam condition with g = 200 near 011 zone axis. The yellow A arrows indicate the dissociated partial dislocations.

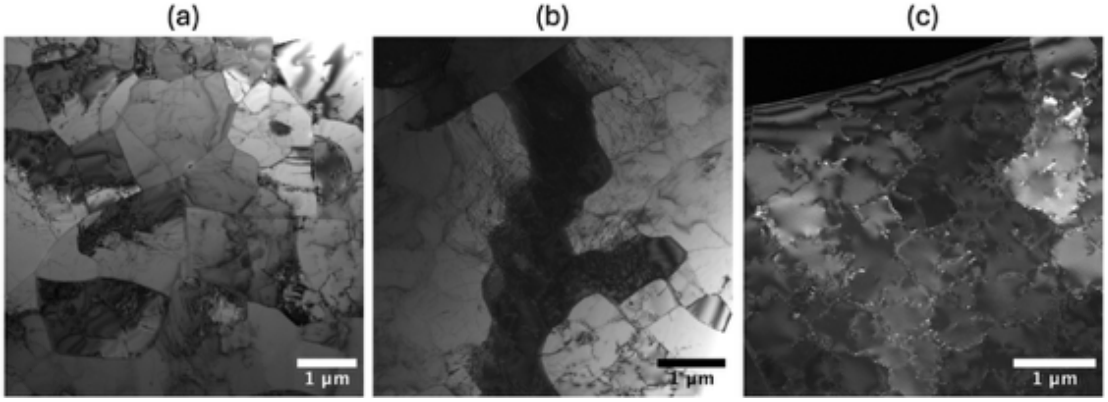

Figure 11. (a and b) BF and (c) DF TEM images of SA LPBF 316H-1. The image condition for the DF image is g = 200 near 011 zone axis.

The BF and DF TEM images of wrought 316L and wrought 316H are shown in Figure 12 and Figure 13, respectively. The dislocation density in the wrought 316 was about 2 orders of magnitude lower than AB LPBF 316H and LPBF 316L, as reported in FY24 [1], and was also lower than those of the SR and SA LPBF 316H. The yellow arrows indicate the dissociated partial dislocations.

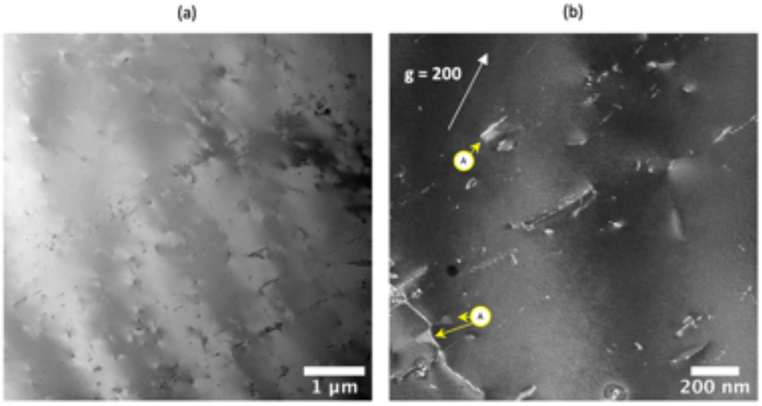

Figure 12. TEM images of as-received wrought 316L: (a) low-magnification BF TEM image. (b) high-magnification DF TEM image in two-beam condition with g = 200 near 011 zone axis. The yellow A arrows indicate the dissociated partial dislocations.

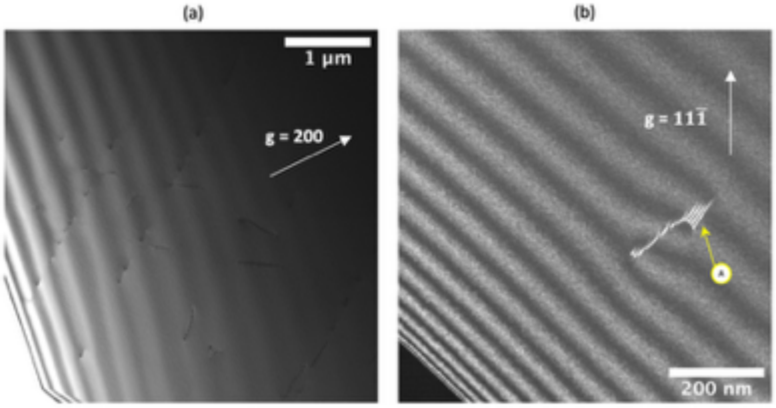

Figure 13. TEM images of as-received wrought 316H: (a) low-magnification BF TEM image in two-beam condition with g = 200 near 011 zone axis. (b) high-magnification DF TEM image in two-beam condition with g = $\mathbf{11\bar{1}}$ near 011 zone axis. The yellow A arrows indicate the dissociated partial dislocations. The fringes across the sample are thickness fringes.

## 3.2 Defect evolution observed with *ex-situ* ion irradiation

This section presents the TEM characterization of ex-situ irradiated LPBF 316H-2 under different processing conditions.

### 3.2.1 Dose dependence of void swelling for SA and SR LPBF 316H

Figure 14 shows the evolution of void swelling in SA and SR LPBF 316H-2 irradiated with 5 MeV Ni ions at 600 °C as a function of dose. Non-irradiated samples were prepared by electropolishing and imaged under two-beam diffraction conditions to reveal the dislocation structure. Irradiated samples were prepared in cross-section by FIB lift-out, tilted to minimize diffraction contrast from dislocations, and defocused by 5 µm to enhance void visibility. For both materials, voids were observed at the first dose of 5 dpa.

Voids within a depth of 400–800 nm from the foil surface were analyzed. Figure 15(a) shows the average void size as a function of dose. The average size increased from 5 dpa to 10 dpa, then slightly decreased from 10 dpa to 15 dpa. Figure 15(b) presents the areal void density as a function of dose. At all doses, SR samples exhibited a higher void density than SA samples. In SR, the density decreased monotonically with increasing dose. In SA, density decreased markedly from 5 dpa to 10 dpa, then increased again at 15 dpa. The drop at 10 dpa appeared too large to be explained solely by variations in foil thickness. Two SA samples were irradiated independently at 10 dpa, yet produced similar results. Further investigation is required to confirm this observation.

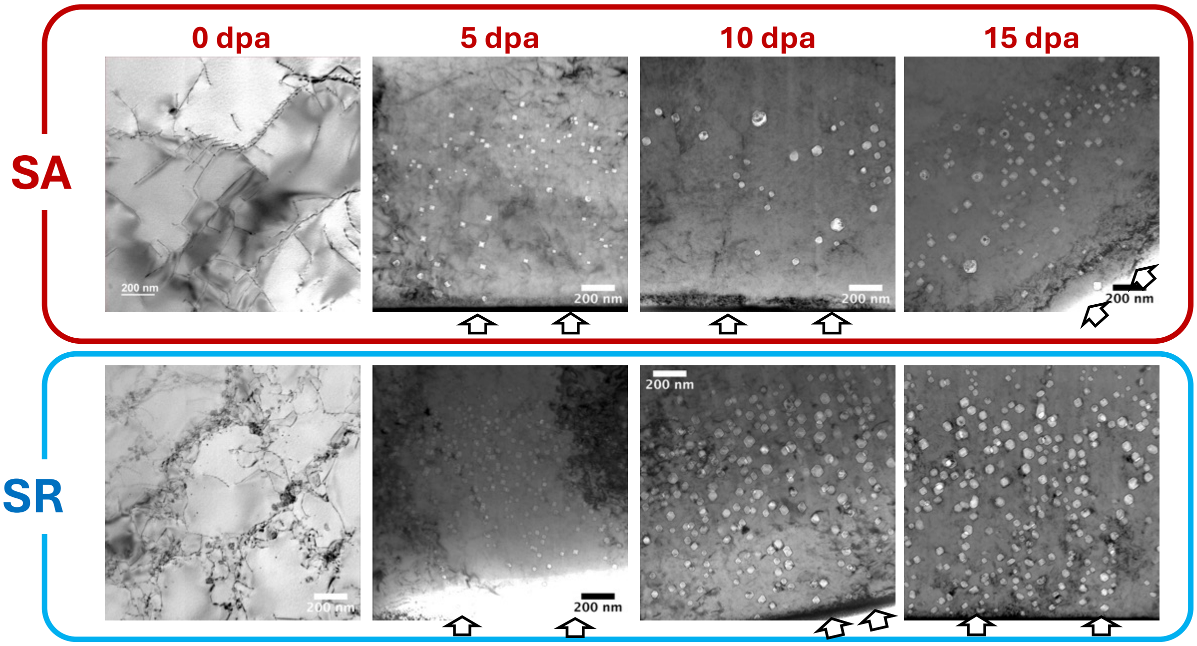

Figure 14. BF cross-sectional TEM images of (top) SA and (bottom) SR LPBF 316H-2 *ex-situ* irradiated at 600°C with 5 MeV $Ni^{2+}$ ions with a dose rate of $10^{-3}$ dpa/s (at 600 nm depth) as a function of dose. The arrows indicate the irradiation direction.

### 3.2.2 Temperature dependence of void swelling for SA and SR LPBF 316H

Figure 16 shows the temperature dependence of void swelling in SA and SR LPBF 316H-2 irradiated with 5 MeV $Ni^{2+}$ ions to 10 dpa. Samples were tilted to reduce diffraction contrast and underfocused to reveal voids. For SA samples, no voids were detected at 400 °C or 500 °C, while at 600 °C and 650 °C, voids were observed at low densities. For SR samples, voids were observed at all four temperatures. Overall, SR samples appeared to exhibit greater swelling than SA samples at all temperatures except 650 °C, where the void density in both materials was similarly low. The temperature dependence of swelling in both SA and SR is generally consistent with that of conventional 316 stainless steels, where peak swelling typically occurs between 600 °C and 650 °C [19].

Voids within 400–800 nm from the foil surface were analyzed. Figure 17 (a) and Figure 17 (b) show the average void size and areal density, respectively, as a function of irradiation temperature. As shown in Figure 17 (a), for SR samples, average void size increased with irradiation temperature up to 600 °C, then slightly decreased from 600 °C to 650 °C. For SA samples, the average size at 650 °C was slightly larger than at 600 °C. A crossover in size between SR and SA samples occurred between 600 °C and 650 °C.

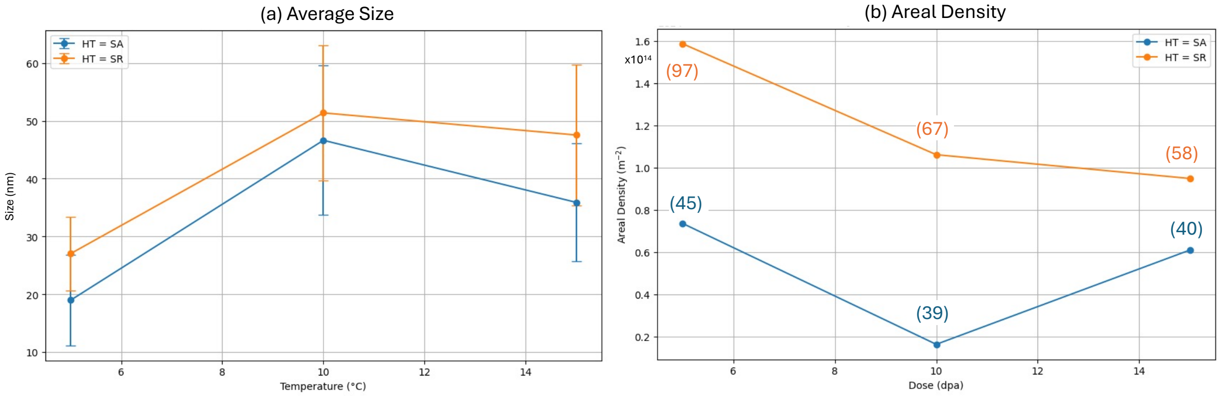

Figure 15. The (a) average size and (b) areal density of voids in SA and SR LPBF 316H-2 irradiated at 600°C with 5 MeV $Ni^{2+}$ ions with a dose rate of $10^{-3}$ dpa/s (600 nm depth) as a function of doses. The error bars correspond to one standard deviation. The numbers in parentheses are the number of cavities measured for individual conditions.

Figure 17(b) shows that for SR samples, void density increased from 400 °C to 500 °C, then decreased with further temperature increases. For SA samples, the areal density was zero at low temperatures until 600°C. The difference in void density between 600 °C and 650 °C was small. Across all temperatures, SR samples maintained higher void densities than SA samples.

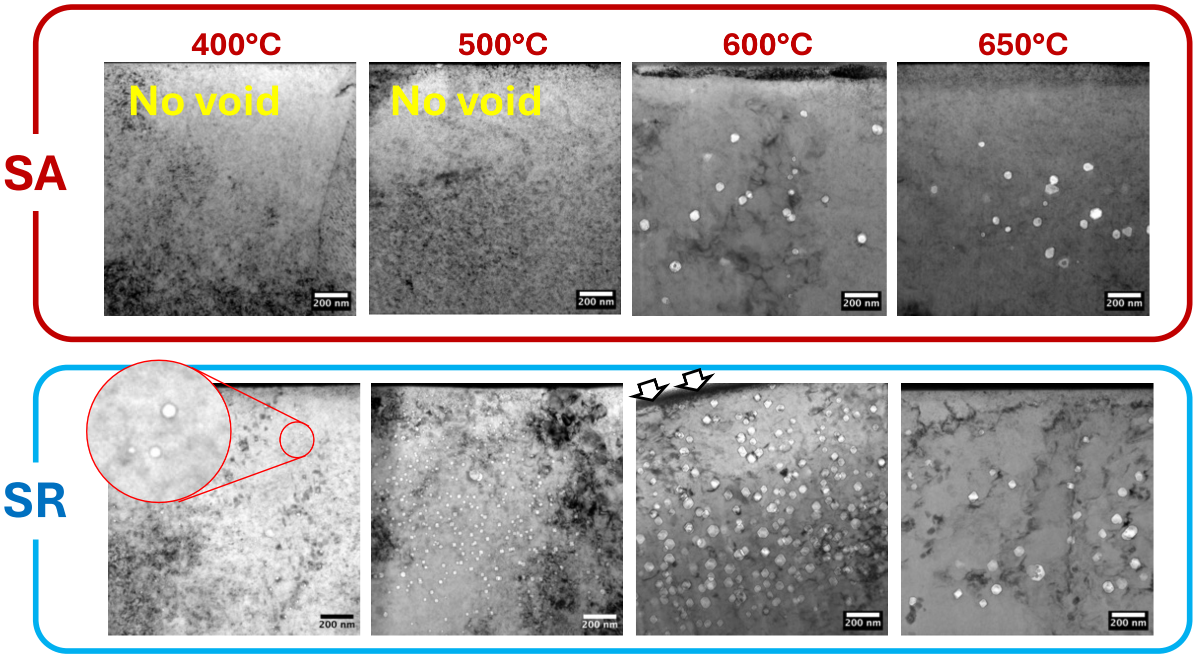

Figure 16. BF cross-sectional TEM images of SA and SR LPBF 316H-2 irradiated with 5 MeV $Ni^{2+}$ ions to 10 dpa with a dose rate of $10^{-3}$ dpa/s (600 nm depth) as a function of irradiation temperatures. The inset image of SR sample at 400°C is a magnified image to show the tiny voids. All samples were irradiated from the top of the image, except for SR LPBF 316H-2 at 600°C where the irradiation direction relative to the image are indicated by the arrows.

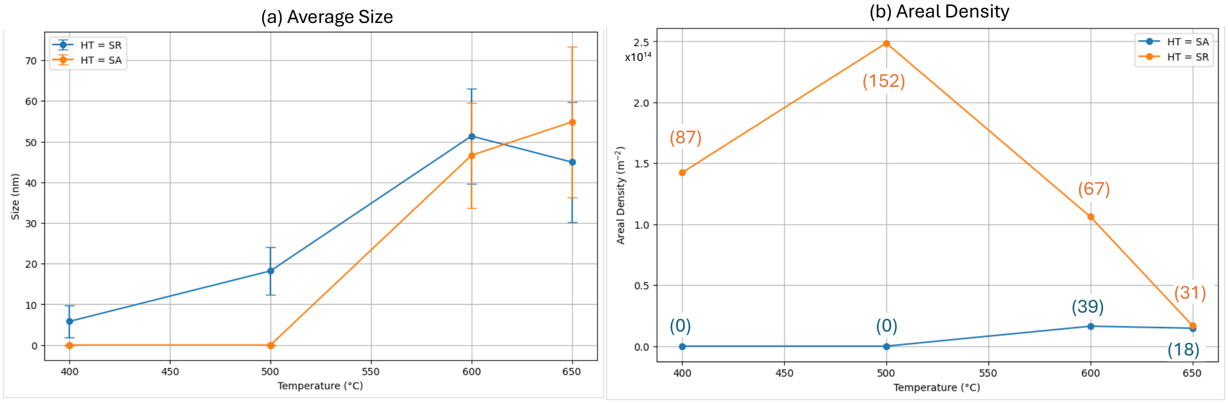

Figure 17. The (a) average size and (b) density of voids in SA and SR LPBF 316H-2 irradiated with 5 MeV $Ni^{2+}$ ions to 10 dpa with a dose rate of $10^{-3}$ dpa/s (600 nm depth) as a function of irradiation temperature. The numbers in parentheses are the number of cavities measured for individual conditions.

### 3.2.3 Comparing the void swelling in LPBF 316H-2 and LPBF 316L-1 under different processing conditions

LPBF 316H-2 specimens with four processing conditions—AB, SR, SA, and 20% CW—were irradiated under identical conditions (5 MeV $Ni^{2+}$ ions, 600 °C, 10 dpa). Figure 18 shows BF TEM images of the four samples before and after irradiation. Non-irradiated samples were prepared by electropolishing and imaged under two-beam diffraction conditions to reveal the dislocation structure. Irradiated samples were prepared in cross-section by FIB lift-out, tilted to minimize diffraction contrast from dislocations, and defocused by 5 µm to enhance void visibility.

The initial dislocation density decreased from left to right in Figure 18. Alternatively, starting from the AB condition, dislocation density increased with CW but decreased with SR and, more markedly, with SA. As shown in Figure 18, both SA and CW samples—representing the lowest and highest dislocation densities, respectively—exhibited less void swelling compared with the intermediate dislocation density AB condition.

Figure 19(a) and Figure 19(b) show the corresponding average void size and areal void density. In terms of void size, the AB sample had the smallest average size, while SR had the largest. For areal density, the AB sample had the highest value, followed by SR. The SA sample ranked third, with a markedly lower density than SR, and the CW sample showed the lowest density overall. The reduced swelling in both SA and CW samples relative to AB and SR was primarily due to their lower void densities.

Figure 20 shows AB and SA LPBF 316L-1 irradiated with 4 MeV $Ni^{2+}$ ions at 600 °C to 10 dpa at a dose rate of $10^{-3}$ dpa/s. The SA sample exhibited significantly lower void swelling than the AB sample. Moreover, no voids were detected in the SA sample irradiated to 5 dpa, whereas voids were clearly present in the 5 dpa AB sample reported previously [18]. Thus, the consistently lower swelling in SA LPBF 316L-1 compared with its AB counterpart was confirmed at both irradiation doses. The darker spherical-shaped contrasts are likely precipitates. Further characterization will be needed to fully determine the nature of those features.

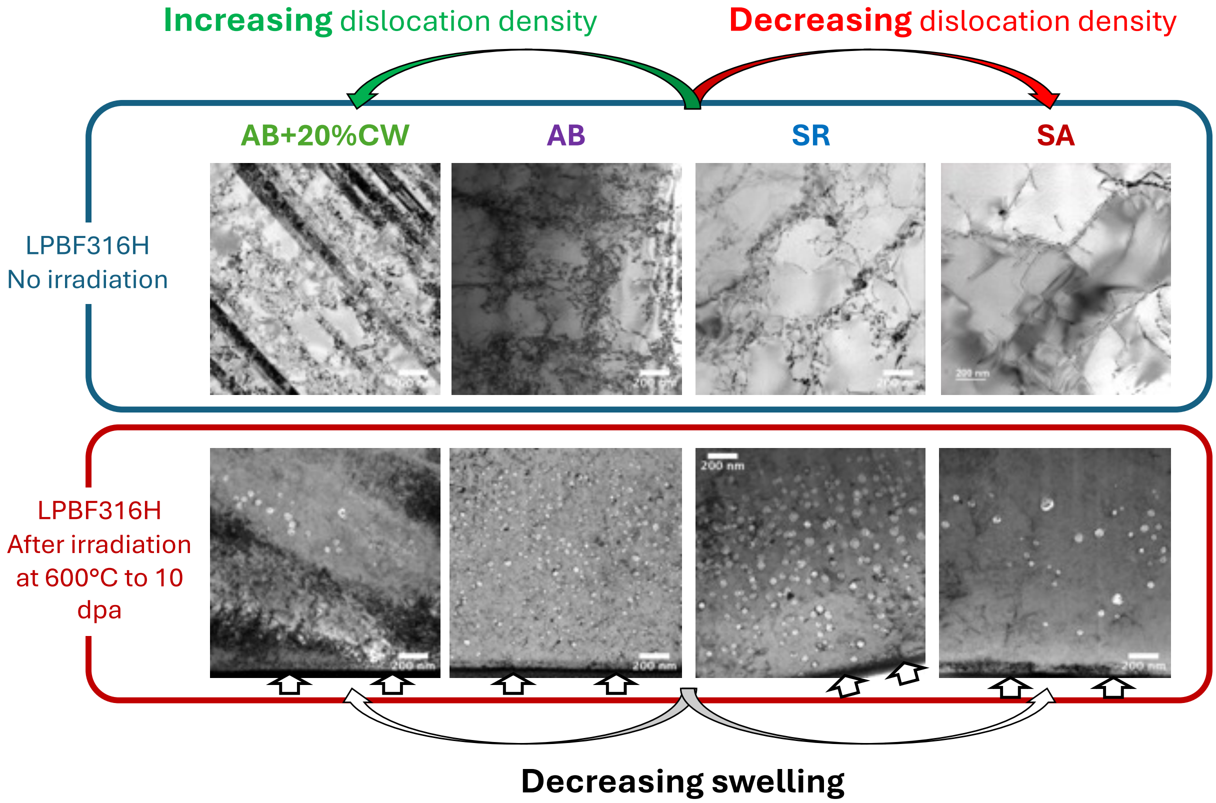

Figure 18. BF TEM images of LPBF 316H-2 with different processing conditions (AB: as built, SR: stress relieved, SA: solution annealed, CW: work worked). Top images are before irradiation. Samples prepared with electropolishing. Lower images are cross-sectional images of samples after irradiation with 5 MeV $Ni^{2+}$ ions at 600°C to 10 dpa with a dose rate of $10^{-3}$ dpa/s (at 600 nm depth).

In our previous reports on AB LPBF 316L-1 and LPBF 316H-1 [1, 18], we showed that void swelling in these materials was noticeably higher than the values reported in the literature for wrought 316 and CW 316 under comparable ion irradiation conditions. We attributed this behavior to the effect of an optimum Q parameter as postulated by Lee and Mansur [20], which suggests that AB LPBF 316 is more susceptible to swelling because its dislocation density falls within a range where the sink strengths of dislocations and cavities are balanced. Thus, dislocation density is the primary factor governing the swelling behavior of LPBF 316 stainless steels. In FY25, we further confirmed the central role of dislocation density by conducting controlled experiments on the same material (LPBF 316H-2 and LPBF 316L-1) processed to different dislocation densities, as shown in Figure 18 to Figure 20.

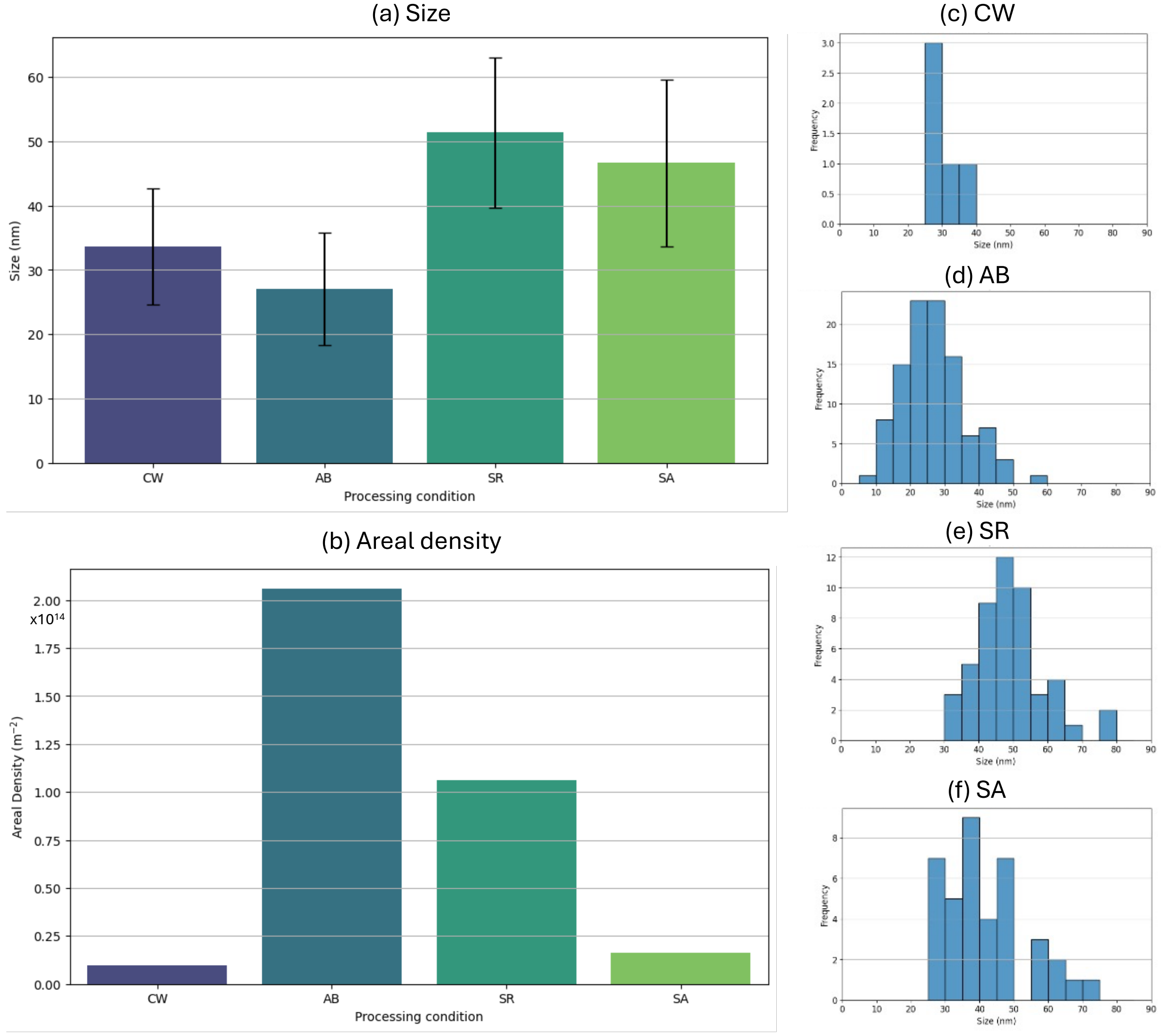

Figure 19. The (a) average size and (b) areal density of voids in LPBF 316H-2 of various processing conditions (AB: as built, SR: stress relieved, SA: solution annealed, CW: work worked) irradiated with 5 MeV $Ni^{2+}$ ions at 600°C to 10 dpa with a dose rate of $10^{-3}$ dpa/s (at 600 nm depth). (c-f) Size distribution of voids.

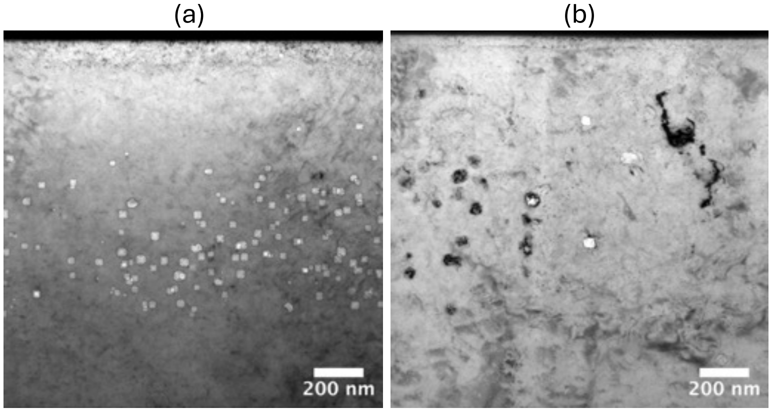

Figure 20. BF TEM images of (a) AB and (b) SA LPBF 316L-1 irradiated with 4 MeV $Ni^{2+}$ ions at 600°C to 10 dpa with a dose rate of $10^{-3}$ dpa/s (at 400 nm depth).

### 3.2.4 Temperature dependence of void swelling of wrought and LPBF 316L and 316H

W316L and W316H were irradiated with 5 MeV Ni ions to compare AB LPBF 316L-1 and LPBF 316H-1, as shown in Figure 21. W316L and W316H were irradiated to 10 dpa at temperatures ranging from 300 °C to 600 °C. No void swelling was observed in either material at 300 °C or 400 °C. Voids were detected at 500 °C and 600 °C.

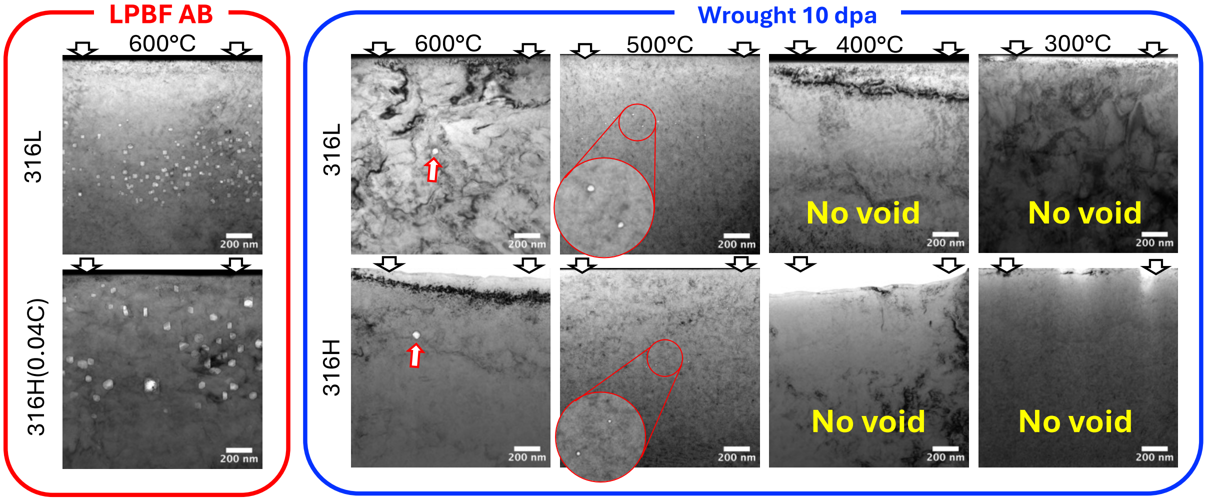

Figure 21. BF cross-sectional TEM images of wrought 316L and 316H stainless steels, AB LPBF 316L-1 and AB LPBF 316H-1 irradiated at various temperatures. The LPBF 316L-1 and LPBF 316H-1 were irradiated with 4 MeV $Ni^{2+}$ ions with a dose rate of $10^{-3}$ dpa/s to 10 dpa (at 400 nm depth), while wrought 316L and 316H were irradiated with 5 MeV $Ni^{2+}$ ions with a dose rate of $10^{-3}$ dpa/s to 10 dpa (at 600 nm depth). The black arrows indicate the direction of the irradiation. The red arrows indicate voids. The circular insets are the magnified image of small voids.

As shown in Figure 22(a), the average void size increased with irradiation temperature. At 500 °C, W316L had a larger average void size than W316H. At 600 °C, only one void was observed in W316H and two in W316L; this difference in size is not statistically significant due to the small number of observed voids. The areal void density, as shown in Figure 22(b), peaked at 500 °C. No voids were detected at 300 °C or 400 °C, and densities were very low at 600 °C.

At 500 °C, the areal void density of W316L was approximately four times higher than that of W316H.

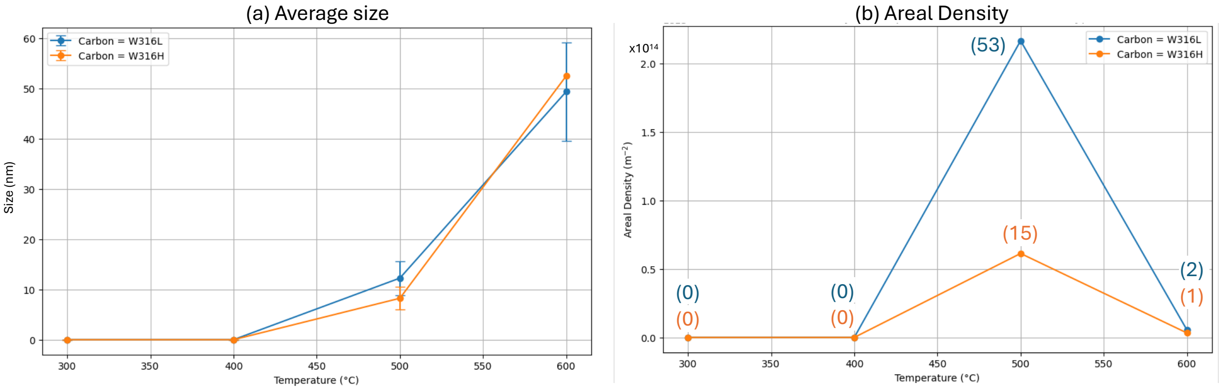

Figure 22. The (a) average size and (b) areal density of voids in wrought 316L and 316H irradiated with 5 MeV $Ni^{2+}$ ions to 10 dpa with a dose rate of $10^{-3}$ dpa/s (at 600 nm depth) as a function of irradiation temperatures. The numbers in parentheses are the number of cavities measured for individual conditions.

When compared to AB LPBF 316L-1 and LPBF 316H-1 irradiated under the same condition (600 °C, 10 dpa), void swelling appeared to be markedly higher in the AB LPBF materials as compared with wrought materials. Among the LPBF alloys, AB LPBF 316L-1 exhibited higher void density but smaller void size than LPBF 316H-1, consistent with previous observations on electropolished plan-view samples [18]. Finally, assuming a foil thickness of 100 nm, Figure 23 shows the swelling comparison between LPBF 316H (0.08 wt.%) with different post-print treatments and wrought 316L and 316H, all irradiated to 10 dpa as a function of irradiation temperature. It shows that solution annealing (reducing dislocation density) and cold working (increasing dislocation density) both reduce swelling in as-built LPBF 316 to a level comparable to wrought materials.

### 3.2.5 Dose rate effect on the void swelling in LPBF 316H and wrought 316H

Figure 24 and Figure 25 compares void swelling in SR and SA LPBF 316H-2 and W316H irradiated at the same temperature under two different dose rates. At the higher dose rate ($10^{-3}$ dpa/s), irradiation to 10 dpa produced void swelling in all three materials, with SR LPBF 316H-2 showing the highest swelling and W316H the lowest. At 2 dpa under this higher dose rate, no voids were observed in any of the materials (as discussed in Section 3.2.7).

At the lower dose rate ($10^{-5}$ dpa/s), as shown in Figure 25, irradiation to just 2 dpa already resulted in measurable void swelling in SR and SA LPBF 316H-2, while W316H showed no voids. For both dose rates, swelling followed the same trend: SR LPBF 316H-2 > SA LPBF 316H-2 > W316H. The absence of voids at 2 dpa for the high dose rate and their presence at 2 dpa for the low dose rate indicate that, for a given accumulated dose, a lower dose rate leads to greater void swelling. This observation is consistent with previous experimental results [21] and with an empirically informed rate-theory modeling study [22], both of which demonstrate that lower dose rates reduce the dose for the onset of high swelling rates.

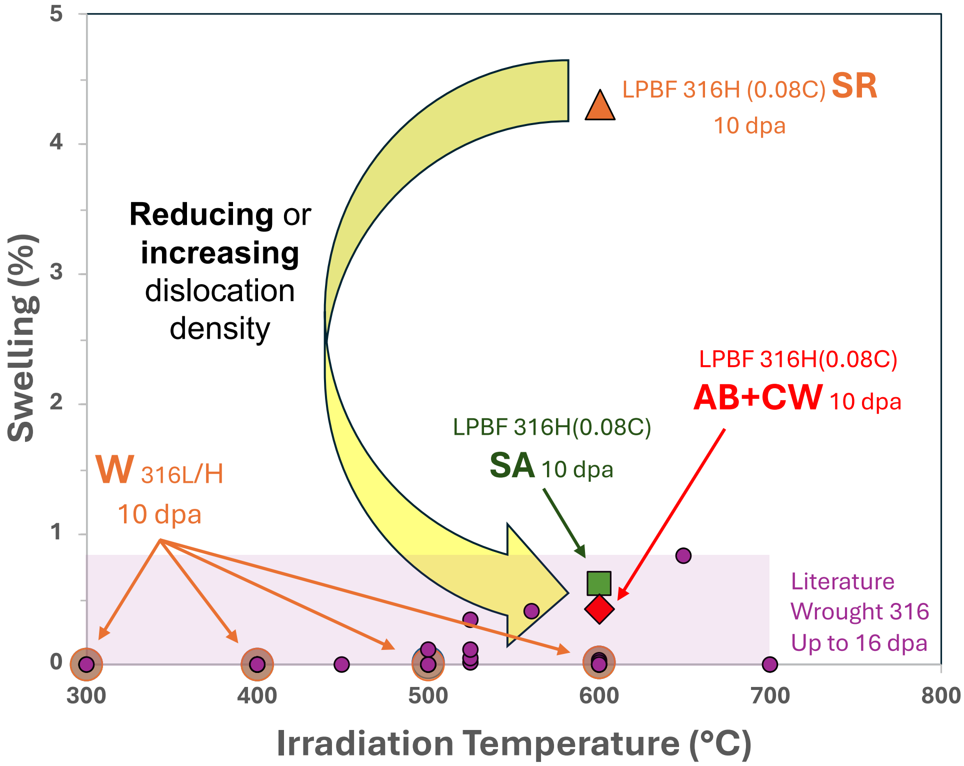

Figure 23. Swelling as a function of irradiation temperatures for SA, SR and CW LPBF 316H-2 and their comparison with wrought materials in this study and from literature. The swelling of the materials of this study is estimated by assuming a TEM foil thickness of 100 nm.

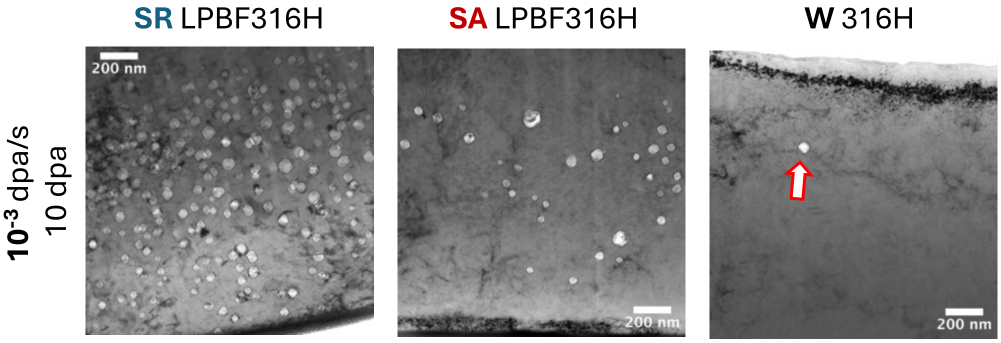

Figure 24. BF cross-sectional TEM images of SR and SA LPBF 316H-2 and wrought 316H irradiated at 600°C with 5 MeV $Ni^{2+}$ ions to 10 dpa with a dose rate of $10^{-3}$ dpa/s

### 3.2.6 Helium effect on the void swelling in SA and SR LPBF 316H

Figure 26 shows TEM images of SA LPBF 316H-2 irradiated at 600 °C with Ni-ion single beam, He-ion single beam, and Ni/He dual beam at ANL. Compared with the Ni-ion-only sample, the dual-beam irradiated samples exhibited significantly greater cavity density. As shown in Figure 26(b) and Figure 26(c), cavities in the dual-beam condition were relatively uniformly distributed. In contrast, the He-only sample (Figure 26d) contained bubbles that were markedly smaller than those in either the Ni-ion-only or dual-beam samples. Moreover, the distribution of bubbles in the He-only sample was highly heterogeneous, being concentrated primarily at dislocations and grain boundaries. Larger bubbles were observed at the helium implantation peak (~600 nm), while smaller bubbles extended to greater depths, particularly along grain boundaries and dislocations. These observations highlight the high mobility of helium and the strong role of dislocations and grain boundaries as diffusion pathways and trapping sites.

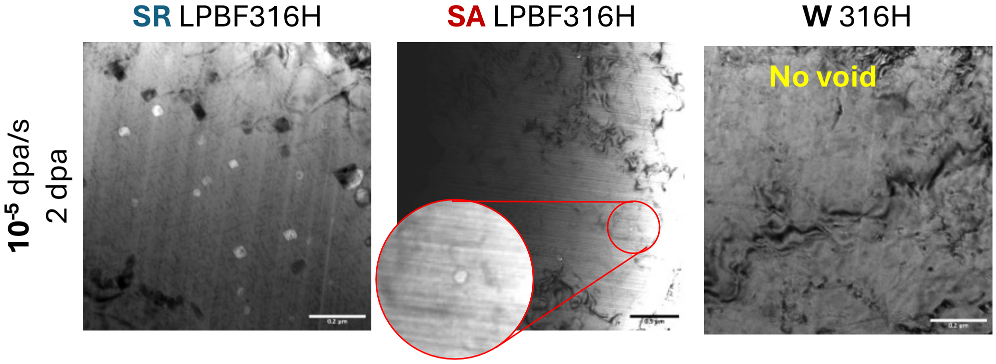

**Figure 25.** BF cross-sectional TEM images of SR and SA LPBF 316H-2 and wrought 316H irradiated at 600°C with 9 MeV $Fe^{3+}$ ions to 2 dpa with a dose rate of $10^{-5}$ dpa/s. The red arrow indicates a void and the red circular inset is a magnified image of a void.

Figure 27(a) and Figure 27 (b) present the corresponding average cavity size and areal density as functions of depth. In the He-only sample, both bubble size and density peaked near a depth of 600–700 nm. For the three samples irradiated with Ni ions (0 appm, 250 appm, and 2500 appm He), between the surface and ~1100 nm depth, the average cavity size decreased while the areal density increased with the amount of He implantation. The dependence of overall swelling is not clear at this point as foil thickness still needs to be measured to calculate the swelling. In the Ni-ion-only sample, void size was relatively insensitive to depth, with the largest cavities appearing near ~1000 nm. In contrast, for the He co-implanted samples, cavity size decreased with depth up to ~600 nm, then increased again until ~1100 nm, while the areal density showed the opposite trend. Beyond 1100 nm, the cavity sizes in all three samples converged and decreased with further depth, with areal density also decreasing. Nevertheless, at all depths, the He co-implanted samples consistently exhibited higher areal cavity densities than the Ni-ion-only sample. These results demonstrate that helium enhances cavity density while suppressing average cavity size.

Figure 28 shows TEM images of SR LPBF 316H-2 irradiated at 600 °C with Ni-ion single beam and Ni/He dual beam. Like the SA samples, helium implantation decreased the average void size while increasing the cavity density. Figure 29 shows TEM images of SA and SR LPBF 316H-2 irradiated with 9 MeV $Fe^{3+}$ and 3.42 MeV $He^{2+}$ at a depth of 1000 nm. Putting the data together, Figure 30(a) and Figure 30(b) present the average void size and areal void density in SA and SR LPBF 316H-2, respectively, measured between 400 and 800 nm depth for 5 MeV $Ni^{2+}$ samples, and between 800 nm to 1200 nm for 9 MeV $Fe^{3+}$ samples. Figure 31 shows the corresponding cavity size distribution. For both SA and SR materials, the average cavity size decreased with increasing helium co-implantation. The effect of helium was more pronounced in SR samples than in SA samples. Without helium, SR exhibited larger average cavity sizes than SA. With 250 appm helium, the average cavity size in SR dropped sharply, becoming smaller than in SA. With further helium addition, the cavity size in SR remained smaller than in SA, though the difference narrowed.

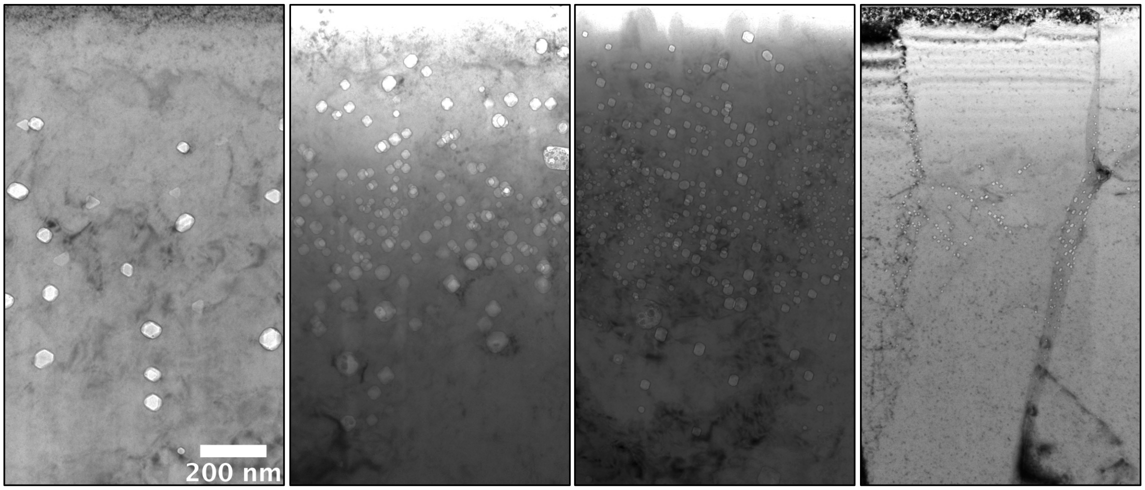

(a) 10 dpa (b) 10 dpa, 250 appm He (c) 10 dpa, 2500 appm He (d) 2500 appm He

Figure 26. BF cross-sectional TEM images of SA LPBF 316H-2 irradiated at 600°C with (a) 5 MeV $Ni^{2+}$ ions only to 10 dpa, (b) 5 MeV $Ni^{2+}$ ions to 10 dpa and 325 keV $He^{+}$ ions to 250 appm, (c) 5 MeV $Ni^{2+}$ ions and 325 keV $He^{+}$ ions to 2500 appm, and (d) 325 keV $He^{+}$ ions only to 2500 appm. The top of the figures is the irradiated surface. The scale bar in (a) applies to all sub-figures. $Ni^{2+}$ ion irradiation achieved 10 dpa at the depth of 600 nm with a dose rate of $10^{-3}$ dpa/s. The top of the figures is the irradiated surface.

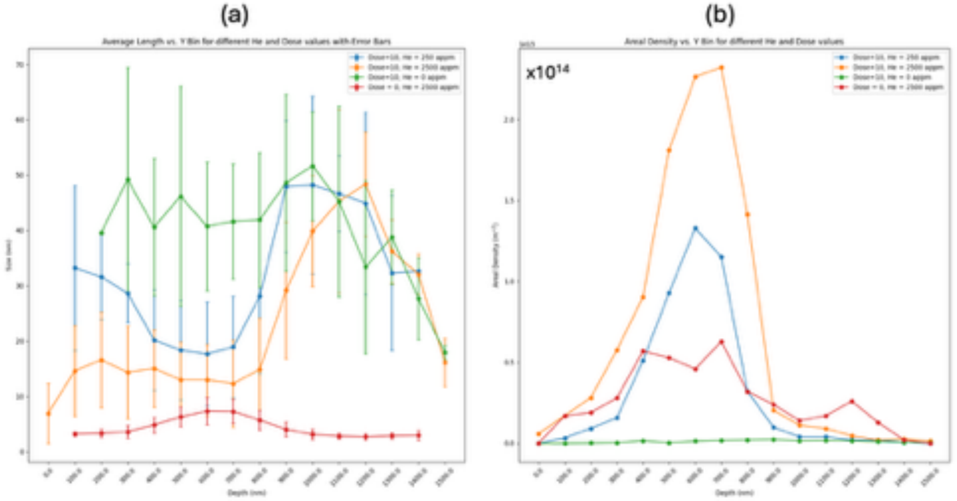

Figure 27. The depth dependence (a) cavity size and (b) cavity areal density in SA LPBF316H-2 irradiated at 600°C with 5 MeV $Ni^{2+}$ ions to 10 dpa with a dose rate of $10^{-3}$ dpa/s (at depth 600 nm) with no He co-implantation, 250 appm $He^{+}$ co-implantation, 2500 appm $He^{+}$ co-implantation, and the sample with only 2500 appm $He^{+}$ implantation.

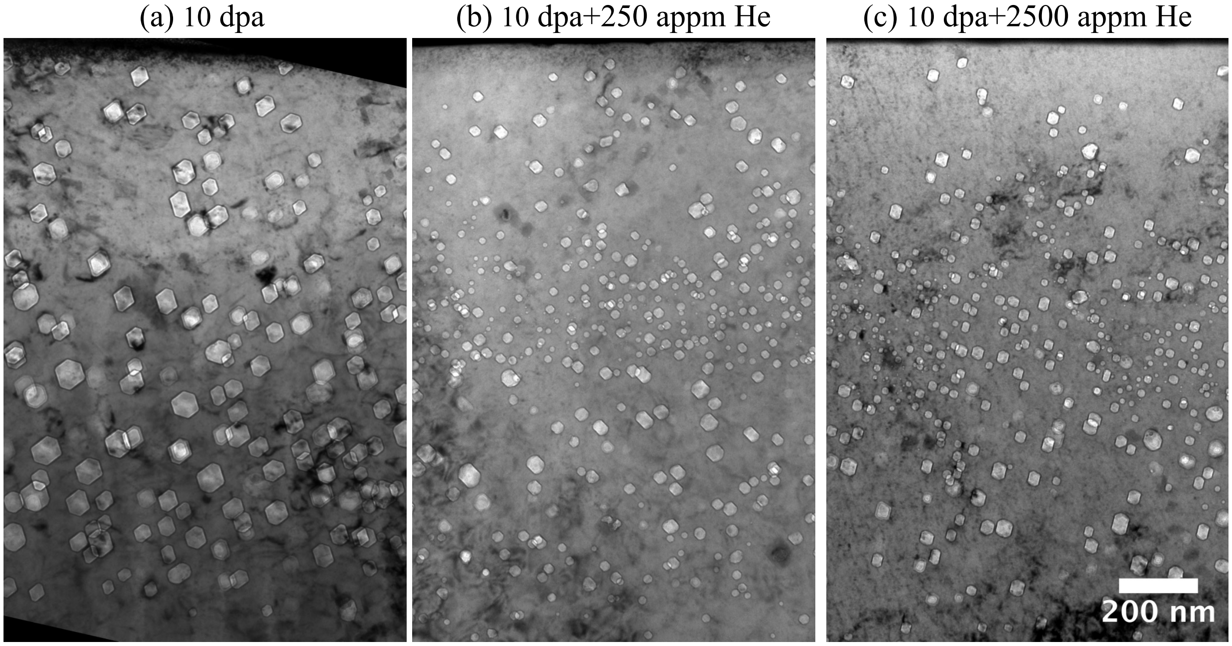

Figure 28. BF cross-sectional TEM images of SR LPBF 316H-2 irradiated at 600°C with (a) only 5 MeV $Ni^{2+}$ ions to 10 dpa, (b) 5 MeV $Ni^{2+}$ ions to 10 dpa and 325 keV $He^{+}$ ions to 250 appm, and (c) 5 MeV $Ni^{2+}$ ions and 325 keV $He^{+}$ ions to 2500 appm. $Ni^{2+}$ ion irradiation achieved 10 dpa at the depth of 600 nm with a dose rate of $10^{-3}$ dpa/s. The top of the figures is the irradiated surface. The scale bar in (c) applies to all sub-figures.

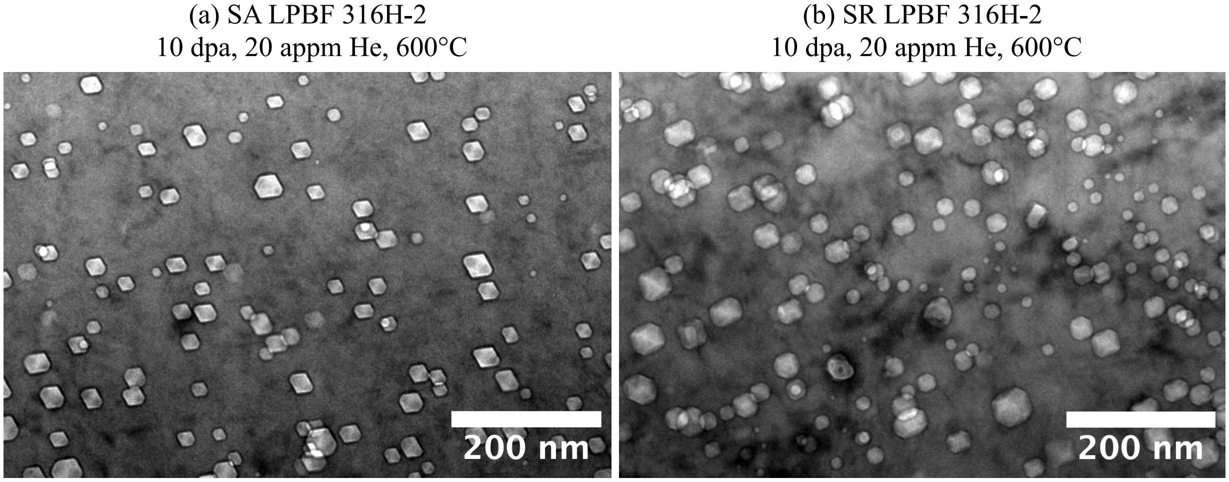

Figure 29. BF cross-sectional TEM images of (a) SA and (b) SR LPBF 316H-2 irradiated at 600°C with 9 MeV $Fe^{3+}$ ions to 10 dpa with a dose rate of $10^{-3}$ dpa/s and 3.42 MeV $He^{2+}$ ions (with degrader) to 20 appm. The images were taken at a depth of 1000 nm.

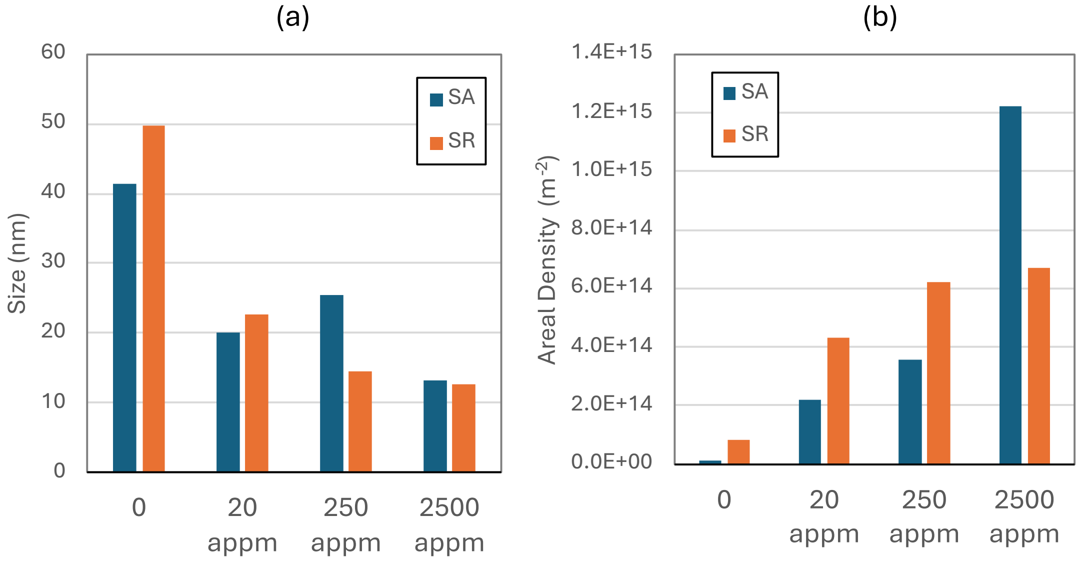

Figure 30. The (a) average size and (b) areal density of voids in SA and SR LPBF316H-2 dual irradiated at 600°C with 5 MeV $Ni^{2+}$ or 9 MeV $Fe^{3+}$ to 10 dpa with a dose rate of $10^{-3}$ dpa/s as a function of concentration of co-implantation of He ions.

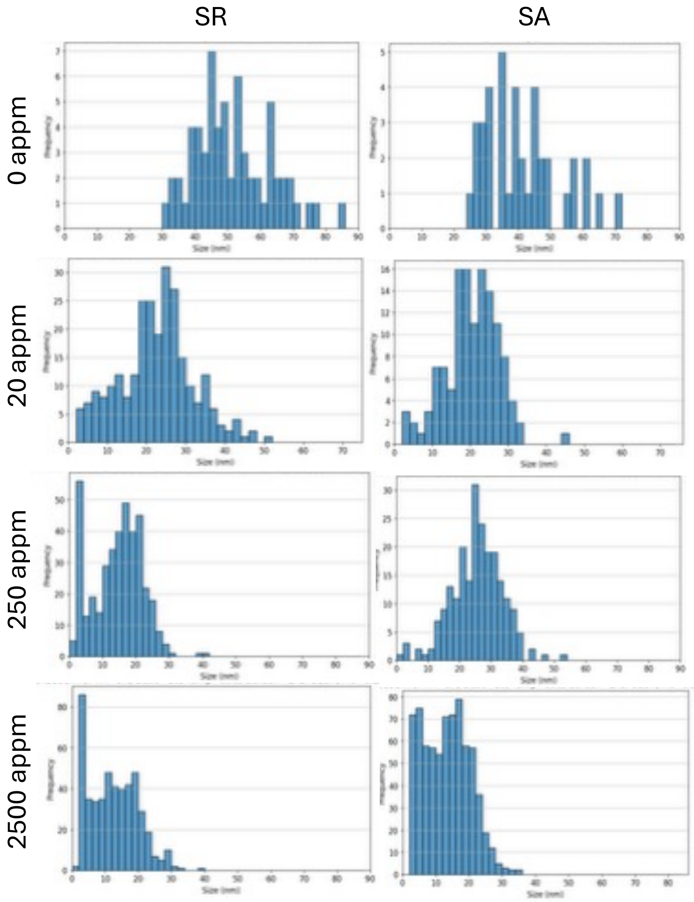

Figure 31. Size distribution of cavities in SA and SR LPBF 316H irradiated at 600°C to 10 dpa as a function of the amount of He co-implantation

In contrast, the areal void density increased with helium co-implantation in both materials, with the SA materials being more sensitive than the SR materials. Due to the lack of foil thickness information, volumetric cavity density could not be conclusively compared between the SA and SR materials. Nonetheless, the current data suggest that helium has a stronger effect on cavity density in SA samples than in SR samples. Further investigation is needed to confirm this trend.

### 3.2.7 Evolution of dislocation loops in SA LPBF 316H

Specimens for examining dislocation loops were prepared by electropolishing. The dislocation structures of irradiated SA LPBF 316H-2 are shown in Figure 32 as a function of temperature and dose. The loop size, measured as the diameter along the long axis, increased with decreasing irradiation temperature and dose. Dislocation-loop denuded zones were observed near grain boundaries in the 400 °C–0.5 dpa sample.

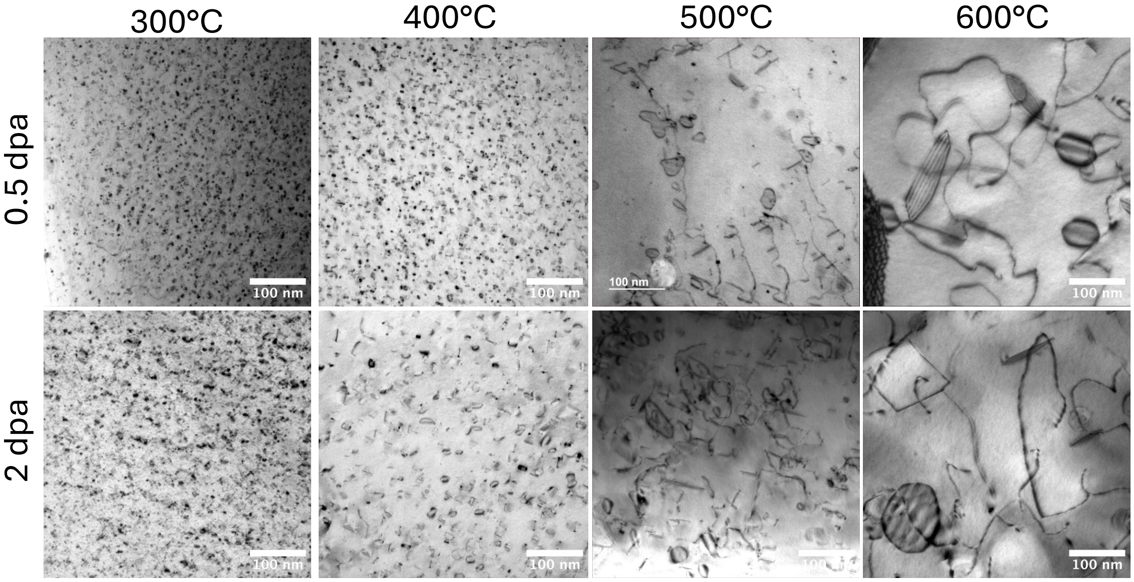

Figure 32. BF TEM images showing the Irradiation-induced dislocation loops in LPBF 316H-2 irradiated with 5 MeV Ni$^{2+}$ ions with a dose rate of $10^{-3}$ dpa/s as a function of temperature and dose.

Figure 33(a) shows an area containing two grain boundaries. The upper boundary (Figure 33b) consists of aligned dislocations; below it, a denuded zone 10–30 nm wide was observed, whereas the denuded zone above the boundary was less pronounced. The lower boundary (Figure 33c), viewed more edge-on, was identified by the diffraction pattern (Figure 33d) as a small-angle grain boundary with a misorientation of ~9°. In contrast, Figure 34 shows denuded zones adjacent to a grain boundary with a higher misorientation. The diffraction pattern on the left indicates the lower grain is near the [110] zone axis with g = 1-11 strongly excited under single-beam conditions, while the pattern on the right shows the upper grain in a multi-beam diffraction condition with an unidentified orientation.

Denuding effects were also observed around isolated pre-existing dislocations. Figure 35 highlights a dislocation in the 400 °C–0.5 dpa sample, with reduced loop density in its vicinity. By contrast, in SA LPBF 316H-2 irradiated at 500 °C to 0.5 dpa, pre-existing dislocations were decorated with dislocation loops, as shown in Figure 36. Both perfect and faulted loops were identified, marked by yellow and red arrows in Figure 36(b), respectively. All four variants of faulted loops were present, as labeled by numbers 1–4. This heterogeneous loop distribution in the 500 °C sample persisted up to at least 2 dpa.

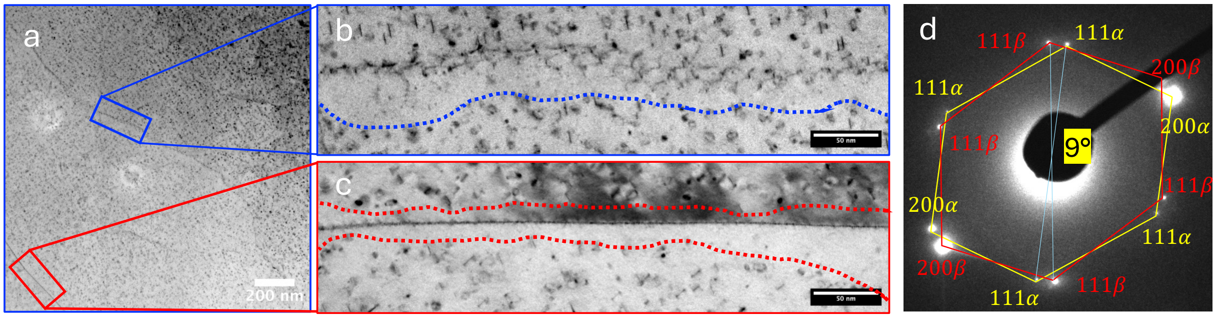

Figure 33. (a) BF TEM image of SA LPBF316H-2 irradiated with 5 MeV Ni$^{2+}$ ions at 400°C to 0.5 dpa with a dose rate of $10^{-3}$ dpa/s. (b,c) enlarged images showing the boundaries of denuded zones near the grain boundaries. (d) diffraction pattern at the lower-left boundary indicating the small orientation difference of 9°.

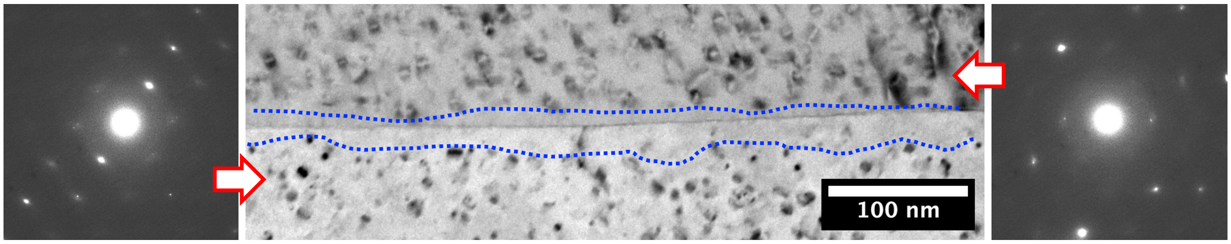

Figure 34. BF TEM image of SA LPBF316H-2 irradiated with 5 MeV Ni$^{2+}$ ions at 400°C to 0.5 dpa with a dose rate of $10^{-3}$ dpa/s. The diffraction patterns on the left and the right correspond to the lower and upper grain, respectively.

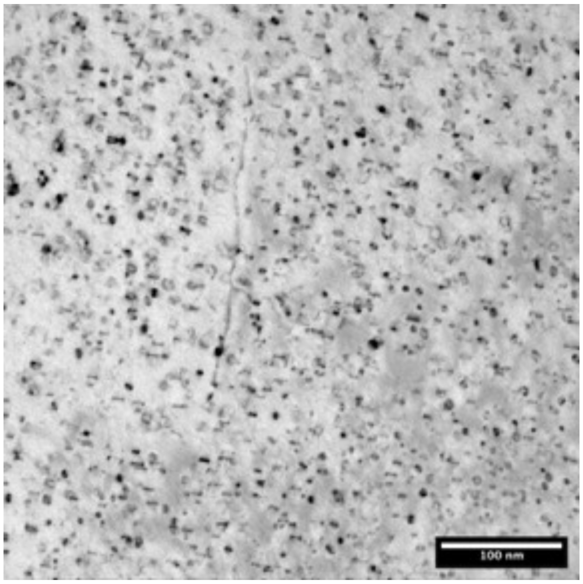

Figure 35. BF TEM image of SA LPBF316H-2 irradiated with 5 MeV Ni$^{2+}$ ions at 400°C to 0.5 dpa. The diffraction patterns on the left and the right correspond to the lower and upper grain, respectively.

For the 600 °C–0.5 dpa sample, as shown in Figure 37, loop decoration was absent at most pre-existing dislocations and dislocation lineups (low angle grain boundaries), with the exception of a single occurrence observed in Figure 33c.

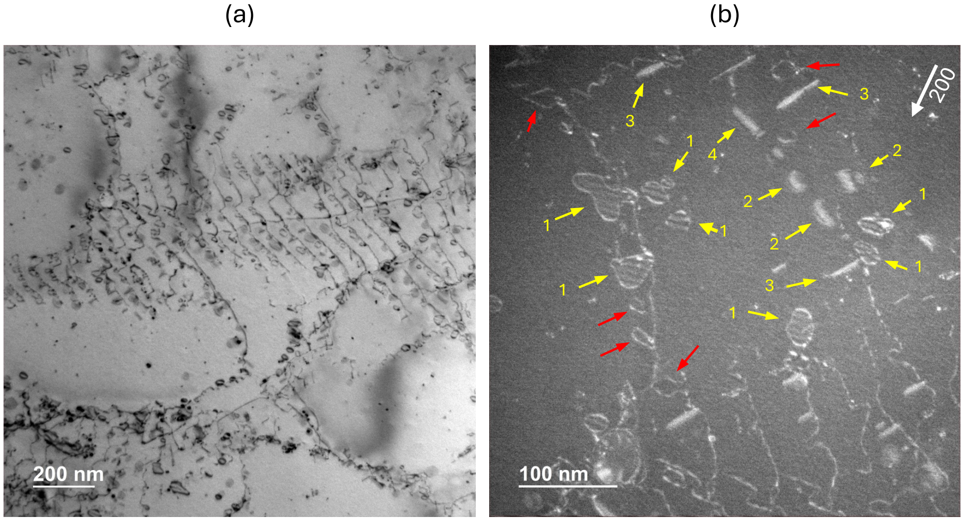

Figure 36. (a) BF and (DF) TEM images of SA LPBF 316H-2 irradiated with 5 MeV Ni$^{2+}$ at 500°C to 0.5 dpa with a dose rate of $10^{-3}$ dpa/s near 011 zone with g = 200. DF image is an enlarged image of the top left corner of the BF image. The red and yellow arrows correspond to perfect and faulted loops, respectively. The numbers indicate the 4 variants of faulted loop orientations.

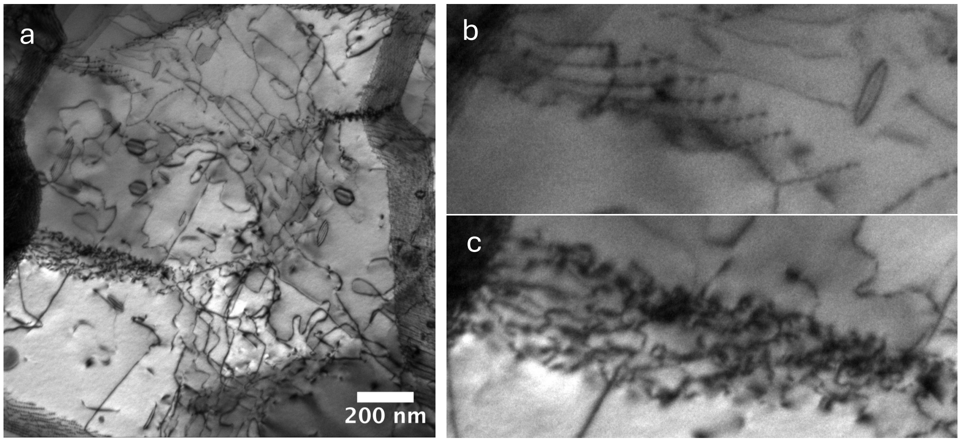

Figure 37. BF TEM image of SA LPBF 316H-2 irradiated with 5 MeV Ni$^{2+}$ at 600°C to 0.5 dpa with a dose rate of $10^{-3}$ dpa/s. (a) low-magnification image. (b) Magnified image of a dislocation line-up without loop decoration. (c) Magnified image of a dislocation line-up with loop decoration.

### 3.2.8 EDS mapping of irradiated LPBF 316H

Figure 38 shows the elemental maps of AB LPBF 316H-2 irradiated with 5 MeV Ni$^{2+}$ ions to 10 dpa at a dose rate of $10^{-3}$ dpa/s. Both irradiated and unirradiated regions are included in the image. In the unirradiated region, the dislocation cell structure was still preserved, indicating annealing a 600°C for about 2.78 hour did not eliminate the dislocation cell structure, although the density may have been reduced. Consistent with previous characterization of LPBF 316H-1 [18], Cr enrichment and Fe depletion were observed at dislocation cell walls. However, unlike LPBF 316H-1, segregation of Mo and Si was not evident. Furthermore, aluminum oxides were observed, but at a low density and without an apparent association with dislocation cells, in contrast to the $MnSiO_3$ particle decorating dislocation cell walls reported previously in LPBF 316H-1 [18] and LPBF 316L [23]. Al content was not provided by vendor powder composition (Table 1). Its effect should be negligible due to the very low particle density.

In the irradiated region, the dislocation cell structure was largely removed. Instead, voids were observed, with Ni enrichment surrounding them, as highlighted in the inset of the Ni map. The Cr segregation and Fe depletion characteristic of dislocation cell walls in the unirradiated region were no longer obvious. Instead, Ni enrichment was detected, likely resulting from irradiation-induced segregation at pre-existing dislocations. The Ni-Si rich precipitates observed previously in LPBF 316H-1 irradiated at 600°C [18] were absent in this sample.

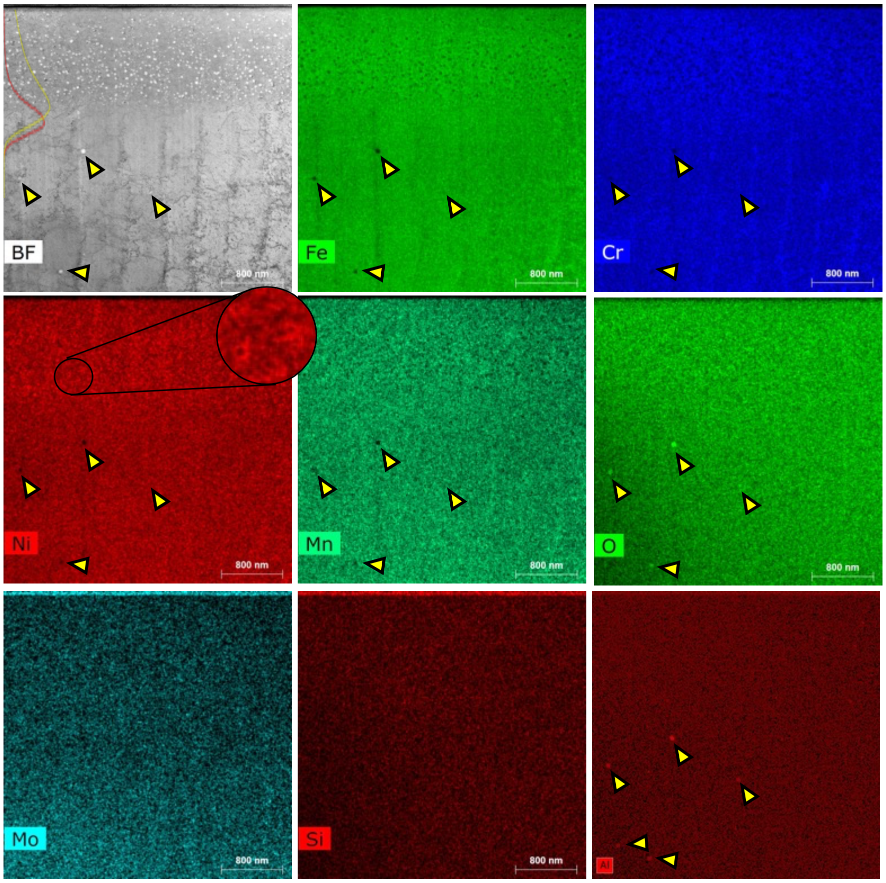

Figure 38. Elemental maps of a cross-sectional sample of AB LPBF 316H-2 irradiated with 5 MeV $Ni^{2+}$ ions at 600°C to 10 dpa with a dose rate of $10^{-3}$ dpa/s (at 600 nm depth). The overlay inset curves in BF subfigure are the ion damage distribution (yellow) and ion range (red). The yellow arrows indicate the oxide particles. The circular inset in Ni map is the enlarged image showing the Ni segregation around voids.

Figure 39 shows the elemental maps of SA LPBF 316H-2 irradiated with 5 MeV $Ni^{2+}$ ions to 10 dpa at a dose rate of $10^{-3}$ dpa/s. Similar to the AB sample, voids were observed with Ni segregation, as highlighted in the enlarged Ni map. The Ni–Si-rich precipitates, as reported previously in irradiated LPBF 316H-1, were not observed either. Aluminum oxides were also detected, as indicated by the arrows. In this sample, some oxides were located within the ion-irradiated region (blue arrows), while others were outside this region (yellow arrows). For oxides outside the irradiated range, the particle sizes matched well between the O/Al maps and the BF image. In contrast, for oxides within the irradiated region, the particle size appeared larger in the BF image than in the O/Al maps, which may be due to ion mixing effects. No carbides were observed in either Figure 38 and Figure 39, as both mappings were performed away from grain boundaries where carbides typically form.

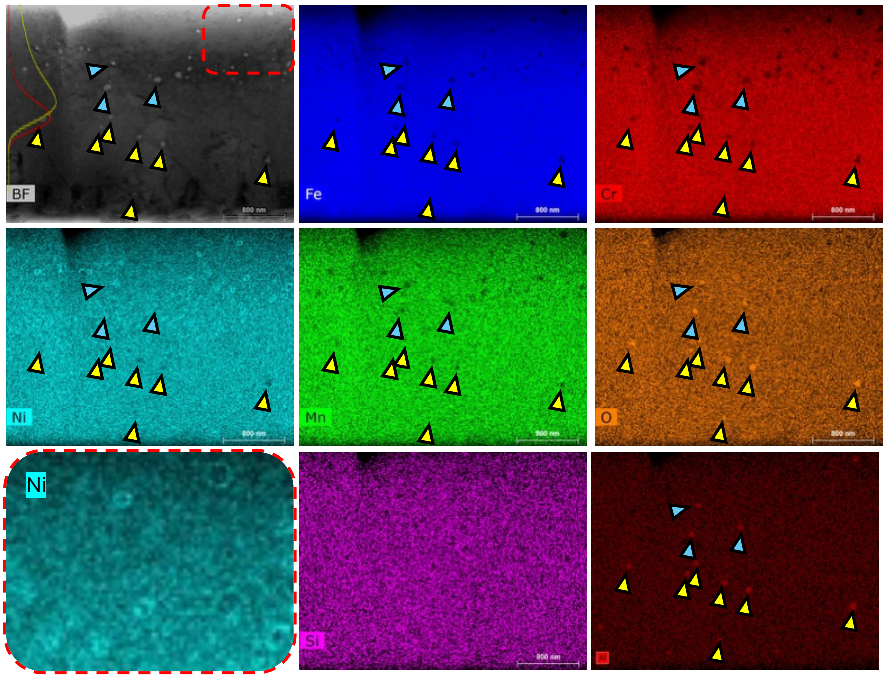

Figure 39. Elemental maps of a cross-sectional sample of SA LPBF 316H-2 irradiated with 5 MeV $Ni^{2+}$ ions at 600°C to 10 dpa with a dose rate of $10^{-3}$ dpa/s (at 600 nm depth). The overlay inset curves in BF subfigure are the ion damage distribution (yellow) and ion range (red). The overlay dashed red box indicate the enlarged area of Ni map. The blue and yellow arrows indicate the oxide particles.

## 3.3 Dislocation loop evolution observed with *in-situ* ion irradiation

Wrought 316L stainless steel was irradiated for comparison with LPBF 316 SS. The defect evolution in wrought 316L was observed under *in-situ* 1 MeV $Kr^{2+}$ ion irradiation at 500°C, 600°C, 625°C and 650°C, as shown in Figure 40. Unlike the LPBF316 stainless steels, where dislocation loop formation is heterogeneous [1], the loop distribution in wrought 316L is uniform. As the temperature increases, the loop density decreases while the loop size increases. However, the variation in dislocation density from 625°C to 650°C was not as significant as that from 600°C to 625°C. Both faulted loops and perfect loops were observed in the wrought material, with no voids detected under any of the conditions tested. A vague alignment of loops is visible for irradiation at 500°C, similar to previous observations in nickel [24]. A quantitative analysis comparing the defect morphology between wrought materials and printed materials is planned for future investigations.

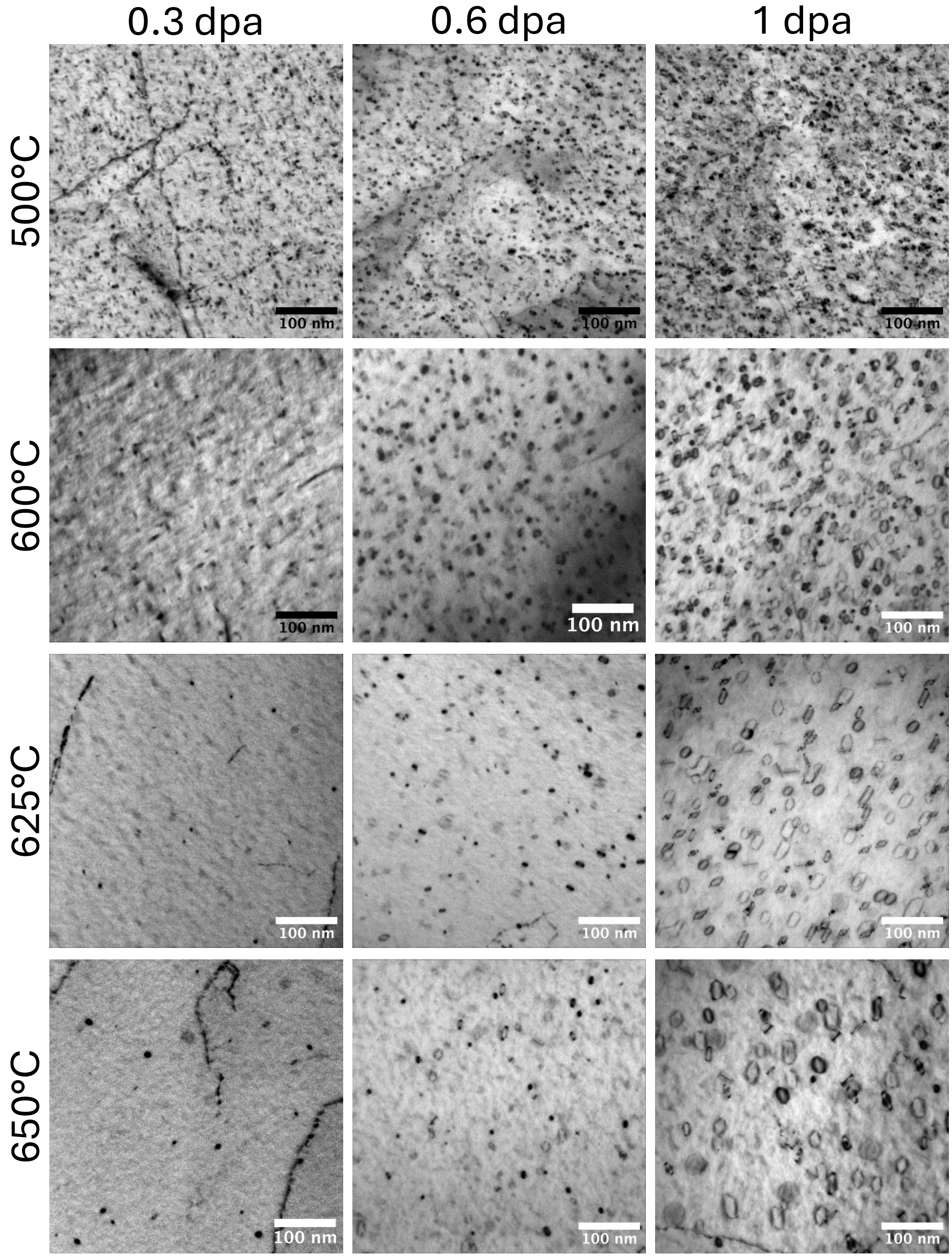

Figure 40. BF images showing the evolution of wrought 316L *in-situ* irradiated with 1 MeV $Kr^{2+}$ ions at 600°C at 500°C, 600°C, 625°C and 650°C to 0.3 dpa, 0.6 dpa and 1 dpa. For 500°C and 600°C, the data were taken from the same area near 011 zone with g = 200. For 625°C, the images were taken from different area where 0.3 dpa and 0.6 dpa were taken near 100 zone with g = 200, and 1 dpa was taken near 110 zone with g = 200. For 650°C, the images were taken from different area but with the same g = 200 near 011 zone.

Similarly, a SA LPBF 316H-1 was in-situ irradiated *in-situ* with 1 MeV $Kr^2$ at 600°C to 0.6 dpa and 1 dpa as shown in Figure 41. The solution annealing treatment removed the dislocation cell structure. Low-angle grain boundaries, such as the one shown in the top-left corner of Figure 41(b), were observed throughout the sample. Faulted and perfect loops were observed uniformly, with loop size increasing as the irradiation dose increased. A denuded zone adjacent to the low-angle grain boundary was also observed, as shown in Figure 41(b), where labels 1 and 2 indicate inclined loops, and 3 and 4 indicate are edge-on loops. Figure 42 shows the loop evolution in SA LPBF 316H-2 *in-situ* irradiated with the same irradiation condition, which shows a similar microstructure as in SA LPBF 316H-1, including the denuded zone for dislocation loops near dislocation alignments.

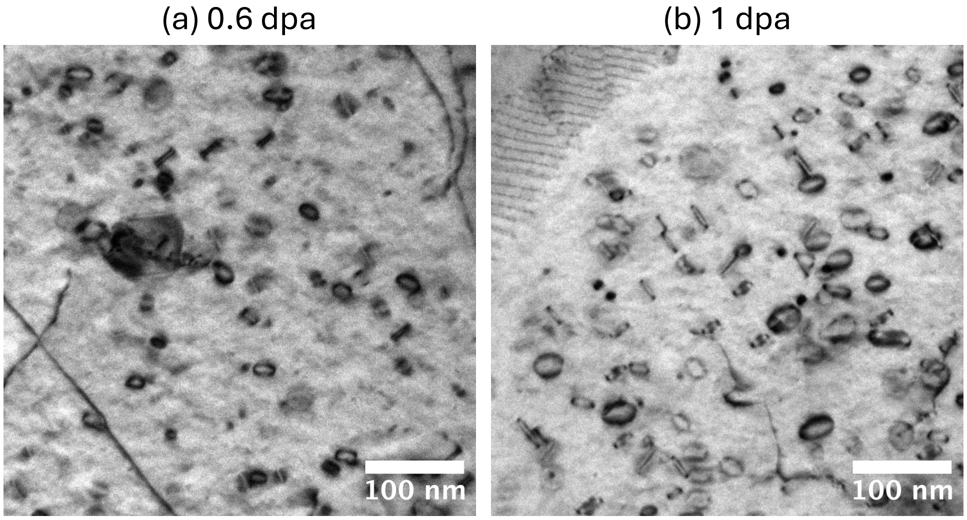

Figure 41. BF images showing the evolution of SA LPBF 316H-1 *in-situ* irradiated with 1 MeV $Kr^{2+}$ ions at 600°C to 0.6 dpa and 1 dpa. The images were taken from different areas with g = 200 near 011 zone axis.

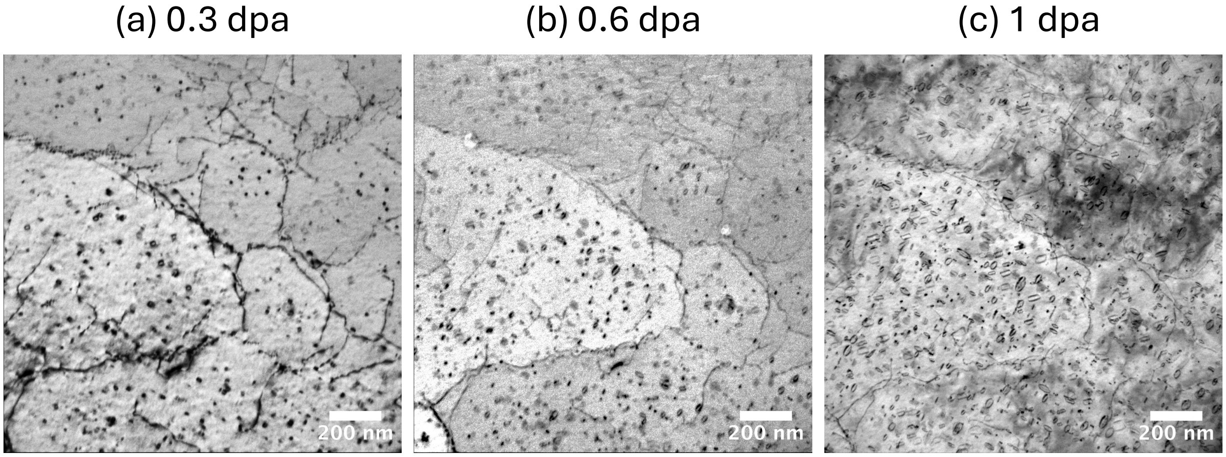

Figure 42. BF images showing the evolution of SA LPBF 316H-2 *in-situ* irradiated with 1 MeV $Kr^{2+}$ ions at 600°C to 0.3 dpa, 0.6 dpa and 1 dpa. The images were taken from the same areas with g = 200 near 001 zone axis.

The *in-situ* experiments indicate that the formation and evolution of dislocation loops in SA LPBF 316H are broadly similar to those in wrought 316. Both materials exhibit uniform loop formation with comparable loop sizes and densities. However, loop-denuded zones adjacent to low-angle grain boundaries (visible as aligned dislocations) were frequently observed in SA LPBF 316H, but not in wrought 316L, consistent with fact that low-angle boundaries are lacking in wrought 316L.

# 4 Summary

This work investigates the effect of heat treatment and processing conditions on the defect evolution and irradiation response of laser powder bed fusion (LPBF) 316H stainless steel, with comparisons to LPBF 316L and wrought 316L/316H. Using complementary *in-situ* and *ex-situ* ion irradiations, we systematically varied temperature (300–675 °C), dose (0.2–25 dpa), dose rate ($10^{-3}$ to $10^{-5}$ dpa/s), and helium co-implantation (20–2500 appm), and correlated the resulting dislocation loops, voids swelling, and segregation with pre-irradiation microstructure controlled by as-built (AB), stress-relieved (SR), solution-annealed (SA), and 20% cold-worked (CW) conditions. The study provides high-fidelity datasets for mechanistic understanding and modeling, supporting the effort of bridging the gap between ion and neutron irradiations.

Pre-irradiation transmission electron microscopy (TEM) characterization revealed that the AB LPBF 316H-2 exhibits a dislocation cell structure, which is partially retained with carbide decoration in SR samples, and replaced by recrystallized grains or low-angle boundaries after SA. CW introduced high dislocation density and slip bands. The relative dislocation density in the examined materials follows the order: CW > AB > SR > SA; $M_{23}C_6$ carbides were only observed in SR samples.

Ex-situ $Ni^{2+}$ ion irradiations revealed that void swelling in LPBF 316H-2 depends strongly on both dose and temperature, as well as dislocation density. At 600 °C, voids appeared by 5 dpa in both SR and SA samples, with SR materials consistently showing larger average void sizes and higher areal densities. As a function of temperature, SR samples developed voids across 400–650 °C, whereas SA samples showed negligible swelling at 400–500 °C and only low-density voids at 600–650 °C. Comparison across AB, SR, SA, and CW conditions at 600 °C and 10 dpa showed that swelling was minimized at the extremes of dislocation sink strength: SA (lowest dislocation density) and CW (highest) both exhibited reduced void densities relative to AB and SR. AB produced the highest void density but the smallest size, while SR had the largest size and second-highest density. These results are consistent with the Q-parameter hypothesis, which predicts that an intermediate dislocation density can maximize swelling susceptibility by balancing the sink strength of cavity and dislocation sink strengths. In contrast, wrought 316L and 316H exhibited much lower swelling under identical conditions, with no voids at 300–400 °C and only low-density voids at 500–600 °C. As summarized in Figure 23, **solution annealing (reducing dislocation density) and cold working (increasing dislocation density) both reduce swelling in as-built LPBF 316 to levels comparable with wrought materials, highlighting dislocation density as a tunable parameter for optimizing 3D-printing and post-processing strategies**.

To extend the relevance of ion irradiation studies to neutron irradiation conditions encountered in nuclear reactors, additional experiments were performed at low dose rates and with helium co-implantation. These parameters were chosen because neutron irradiation in reactors typically occurs at lower dose rates and involves helium production via transmutation, both of which can significantly affect defect evolution and swelling behavior. By replicating these conditions in ion irradiation experiments, the study aims to bridge the gap between accelerated ion testing and actual reactor service environments.

Low-dose-rate ($10^{-5}$ dpa/s) experiments revealed that swelling onset occurs at lower doses, consistent with rate-theory predictions and previous neutron irradiation results. The relative swelling in SA, SR and wrought materials irradiated with low dose rate was consistent with the trend observed with higher dose rate ($10^{-3}$ dpa/s), which indicates that **the swelling mitigation**

**strategy discussed above (tuning the dislocation density) remains applicable when extended to the reactor-relevant dose rate.**

Helium co-implantation ($Ni^{2+}/He^{+}$ or $Fe^{3+}/He^{2+}$ dual-beam at 600 °C) increased cavity areal density while decreasing average cavity size in both SA and SR, indicating enhanced cavity nucleation by He. He-only implantation produced small, heterogeneous bubbles concentrated at dislocations and grain boundaries, whereas dual-beam conditions yielded more uniform cavities. The decrease in void size with He was stronger in SR; the increase in areal density with He was stronger in SA. While final volumetric swelling quantification awaits foil thickness measurements, the combined data indicate that He promotes cavity formation and can enhance swelling. With helium present, the difference in overall swelling between SA and SR 316 was reduced, **indicating that the transmutation-produced helium weakens the role of dislocation density in swelling control and drives LPBF 316 stainless steels toward swelling behavior more similar to that of wrought alloys.**

*In-situ* irradiation experiments revealed distinct differences and similarities between wrought 316L and SA LPBF 316H stainless steels. Wrought 316L irradiated with 1 MeV $Kr^{2+}$ ions at 500–650 °C exhibited uniform dislocation loop formation, with decreasing density and increasing size at higher temperatures. In contrast, SA LPBF 316H-1 and 316H-2 irradiated under similar conditions also showed uniform distributions of faulted and perfect loops, with loop size increasing with dose, but additionally exhibited loop-denuded zones near low-angle grain boundaries formed by aligned dislocations. These results suggest that while loop formation in SA LPBF 316H is broadly similar to wrought 316L, the presence of low-angle grain boundaries in the LPBF material introduces localized heterogeneities absent in the wrought counterpart.

*Ex-situ* 5 MeV $Ni^{2+}$ ion irradiated SA LPBF 316H-2 exhibited temperature- and dose-dependent dislocation loop evolution, with loop size increasing with temperatures and doses. At 400 °C–0.5 dpa, denuded zones formed near grain boundaries and around isolated dislocations, while at 500 °C–0.5 dpa, pre-existing dislocations were decorated with both perfect and faulted loops, yielding a heterogeneous distribution that persisted up to 2 dpa. By contrast, at 600 °C–0.5 dpa, loop decoration was largely absent, with only rare occurrences near low-angle grain boundaries.

STEM-EDS mapping after 5 MeV $Ni^{2+}$ ion irradiation to 10 dpa revealed Ni enrichment around voids in both AB and SA LPBF 316H-2, consistent with irradiation-induced segregation; Cr enrichment at AB cell walls was evident only in unirradiated regions. Unlike prior observations in a different LPBF 316H lot, Ni–Si precipitates were not observed; sparse Al-rich oxides were detected without a clear association with prior cell walls.

Collectively, the results show that dislocation density (controlled by post-printing processing), helium content, and dose rate are the factors influencing swelling in LPBF 316H. Swelling can be minimized either by reducing dislocation density via solution annealing or by increasing it via cold work; LPBF 316H with intermediate dislocation densities (e.g., AB, SR) are most susceptible to swelling. Helium and lower dose rates both lower the incubation dose and increase cavity populations. Wrought 316L/316H remain less swelling-prone than LPBF under ion irradiation. The combined *in-situ*/*ex-situ* datasets provide mechanistic inputs and validation targets for cluster dynamics and phase-field models that bridge ion to neutron conditions, directly supporting LAIN and the accelerated qualification of AM austenitic steels for nuclear service. Ongoing work includes volumetric swelling quantification via foil-thickness measurements, quantitative loop/cavity statistics, and stronger connections to HFIR/ATR neutron irradiation data.

# 5 Acknowledgements

This work was sponsored by the U.S. Department of Energy, Office of Nuclear Energy, Advanced Materials and Manufacturing Technologies (AMMT) program, under Contract No. DE-AC02-06CH11357 with Argonne National Laboratory, managed and operated by UChicago Argonne LLC. Dr. Xuan Zhang from Argonne National Laboratory and Dr. Caleb Massey from Oak Ridge National Laboratory are thanked for providing the materials used for this study. Dr. Andrea Jokisaari and Dr. Rongjie Song, Dr. Sourabh Kadambi, Dr. Sanjoy Mazumder, and Dr. Mattew Swisher from Idaho National Laboratory are thanked for the fruitful discussion. Prof. Stubbins and Mr. Mahmud Ovi from University of Illinois are thanked for performing the cold working. Prof. Kevin Field, Dr. Kai Sun and Mr. Hangyu Li from University of Michigan are thanked for performing low dose rate ion irradiation, dual beam ion irradiation, and FIB sample preparation. The low dose irradiation and dual beam ion irradiation was supported by the U.S. Department of Energy, Office of Nuclear Energy under DOE Idaho Operations Office Contract DE-AC07-05ID14517 as part of Nuclear Science User Facilities awards #24-4964 and #24-4838. Prof. Shunyu Liu from Clemson is thanked for aiding sample preparation. The Work performed at the Center for Nanoscale Materials, a U.S. Department of Energy Office of Science User Facility, was supported by the U.S. DOE, Office of Basic Energy Sciences, under Contract No. DE-AC02-06CH11357.

# 6 References

[1] W.-Y. Chen, Y. Chen, P. Baldo, L. Gao, D. Harbaruk, J. Hlavenka, In-situ and ex-situ characterization of irradiated AM materials, Argonne National Laboratory (ANL), Argonne, IL (United States), 2024.
[2] S.B. Kadambi, M. Swisher, S. Mazumder, W.T. Yorgason, A.M. Jokisaari, Interpretation of Ion Irradiation and Neutron Irradiation Damage in Additively Manufactured 316 Stainless Steel using Multiscale Modeling, Idaho National Laboratory (INL) INL/RPT-25-87879 (2025).
[3] A.M. Jokisaari, S.B. Kadambi, S.K. Mazumder, M.M. Swisher, W.T. Yorgason, Defect Production and Microstructural Feature Impact for Radiation Damage in Additively Manufactured 316 Stainless Steel, Idaho National Laboratory (INL), Idaho Falls, ID (United States), 2024.
[4] S. Taller, Y. Chen, R. Song, W.-Y. Chen, A. Jokisaari, An approach to combine neutron and ion irradiation data to accelerate material qualification for nuclear reactors, Journal of Nuclear Materials 603 (2025) 155385.
[5] C. Massey, P. Nandwana, H. Hyer, S. Nayir, J. Kendall, C. Joslin, R. Duncan, D. Collins, T.G. Seibert, F. List III, Data-Driven Optimization of the Processing Window for 316H Components Fabricated Using Laser Powder Bed Fusion, Oak Ridge National Laboratory, ak Ridge National Laboratory (2023).
[6] T. Byun, B.E. Garrison, M.R. McAlister, X. Chen, M.N. Gussev, T.G. Lach, A. Le Coq, K. Linton, C.B. Joslin, J.K. Carver, Mechanical behavior of additively manufactured and wrought 316L stainless steels before and after neutron irradiation, Journal of Nuclear Materials 548 (2021) 152849.
[7] X. Zhang, S.A. Mantri, G. Vukovic, J. Listwan, D. Rink, E. Listwan, Development of process parameters and post-build conditions for qualification of LPBF 316 SS, ANL-AMMT-004, (2023).
[8] W.-Y. Chen, Y. Chen, P. Baldo, J. Hlavenka, D. Harbaruk, In-situ and ex-situ characterization of ion-irradiated AM materials, ANL-AMMT-005, Argonne National Laboratory (ANL), Argonne, IL (United States), 2023.
[9] T.S. Byun, D.A. Collins, A.G. Le Coq, T.G. Lach, K.D. Linton, M.N. Gussev, J.W. Werden, M.R. Mcalister, X. Chen, C.B. Joslin, Mechanical Properties of Additively Manufactured 316L Stainless Steel Before and After Neutron Irradiation (FY21), Oak Ridge National Lab.(ORNL), Oak Ridge, TN (United States), 2021.
[10] P. Champlin, C. Massey, A. Le Coq, S. Taller, T. Byun, K. Linton, AMMT FY23 HFIR Irradiation Test Matrix–Supported by the Design of a Miniature Bend Bar Irradiation Vehicle, Oak Ridge National Laboratory (ORNL), Oak Ridge, TN (United States), 2023.
[11] M. Li, D. Andersson, R. Dehoff, A. Jokisaari, I. van Rooyen, D. Cairns-Gallimore, Advanced materials and manufacturing technologies (AMMT) 2022 roadmap, Argonne National Lab.(ANL), Argonne, IL (United States), 2022.
[12] X. Zhang, S.A. Mantri, G.I. Vukovic, J. Listwan, D. Rink, E. Listwan, Development of process parameters and post-build conditions for qualification of LPBF 316 SS. ANL-AMMT-004, Argonne National Laboratory (ANL), Argonne, IL (United States), 2023.
[13] M. Li, W.-Y. Chen, P.M. Baldo, In situ transmission electron microscopy with dual ion beam irradiation and implantation, Materials Characterization 173 (2021) 110905.
[14] J.F. Ziegler, M.D. Ziegler, J.P. Biersack, SRIM–The stopping and range of ions in matter (2010), Nuclear Instruments and Methods in Physics Research Section B: Beam Interactions with Materials and Atoms 268(11-12) (2010) 1818-1823.
[15] W.-Y. Chen, X. Liu, Y. Chen, J.-W. Yeh, K.-K. Tseng, K. Natesan, Irradiation effects in high entropy alloys and 316H stainless steel at 300 C, Journal of Nuclear Materials 510 (2018) 421-430.
[16] S. Taller, F. Naab, G.S. Was, A methodology for customizing implantation profiles of light ions using a single thin foil energy degrader, Nuclear Instruments and Methods in Physics Research Section B: Beam Interactions with Materials and Atoms 478 (2020) 274-283.

[17] S. Taller, D. Woodley, E. Getto, A.M. Monterrosa, Z. Jiao, O. Toader, F. Naab, T. Kubley, S. Dwaraknath, G.S. Was, Multiple ion beam irradiation for the study of radiation damage in materials, Nuclear Instruments and Methods in Physics Research Section B: Beam Interactions with Materials and Atoms 412 (2017) 1-10.
[18] W.-Y. Chen, S. Taller, A.M. Jokisaari, C. Yiren, R. Song, X. Zhang, L. Gao, P.M. Baldo, D. Habaruk, M. Li, Characterization of in-situ and ex-situ Ion-Irradiated Additively Manufactured 316L and 316H Stainless Steels, Journal of Nuclear Materials (2025) 156044.
[19] M. Terasawa, S. Nakahigashi, H. Kamei, T. Takeyama, S. Ohonuki, H. Takahashi, Void swelling and microchemical segregation in ion-irradiated 316 stainless steel, Journal of Nuclear Materials 104 (1981) 1017-1021.
[20] E. Lee, L. Mansur, Unified theoretical analysis of experimental swelling data for irradiated austenitic and ferritic/martensitic alloys, Metallurgical Transactions A 21(4) (1990) 1021-1035.
[21] F. Garner, S. Porollo, Y.V. Konobeev, O. Maksimkin, Void swelling of austenitic steels irradiated with neutrons at low temperatures and very low dpa rates, Proceedings of the Twelfth International Conference on Environmental Degradation of Materials in Nuclear Power Systems-Water Reactors, 2005, pp. 439-448.
[22] M. Griffiths, J. Ramos-Nervi, L. Greenwood, A rate theory model of radiation-induced swelling in an austenitic stainless steel, Journal of Nuclear Engineering 2(4) (2021) 484-515.
[23] Y.M. Wang, T. Voisin, J.T. McKeown, J. Ye, N.P. Calta, Z. Li, Z. Zeng, Y. Zhang, W. Chen, T.T. Roehling, Additively manufactured hierarchical stainless steels with high strength and ductility, Nature materials 17(1) (2018) 63-71.
[24] W.-Y. Chen, M. Li, Helium bubble formation in nickel under in-situ krypton and helium ions dual-beam irradiation, Journal of Nuclear Materials 558 (2022) 153342.

**Nuclear Science and Engineering Division**
Argonne National Laboratory
9700 South Cass Avenue, Bldg. 212
Argonne, IL 60439

www.anl.gov

Argonne National Laboratory is a U.S. Department of Energy
laboratory managed by UChicago Argonne, LLC